The Asteroid-Comet Continuum[1]

David Jewitt

Department of Earth, Planetary and Space Sciences, University of California at Los Angeles

Henry H. Hsieh

Planetary Science Institute, Honolulu

The practical distinctions between asteroids and comets, viewed as products of accretion on either side of the snow line, are less clear-cut than previously understood. In this chapter, we discuss the numerous solar system populations which have physical and dynamical properties that conflict with any simple diagnosis of their nature and origin. Studies of these so-called "continuum" or "transition objects", which include many of the most intriguing bodies in the solar system, have implications for a broad range of scientific topics from the demise of comets and the activation of asteroids to the production of interplanetary debris and the origin of the terrestrial planet volatiles. We present an overview of the current state of knowledge concerning the asteroid-comet continuum and discuss the numerous physical processes behind the activity shown by small bodies in the solar system.

1. INTRODUCTION

Traditionally, small solar system bodies have been classified as either asteroids (complex assemblages of refractory minerals) or comets (ice rich bodies containing a mix of volatile and refractory solids). Observationally, asteroids and comets are differentiated by the absence or presence of detectable mass loss. Comets, in essence, appear fuzzy while asteroids do not. Cometary activity typically takes the form of comae (unbound ejected material surrounding the central body) and tails.

Meanwhile, the classical dynamical distinction between comets and asteroids is based on the Tisserand parameter (with respect to Jupiter),

$$T_J = \frac{a_J}{a} + 2\left[(1-e^2)\frac{a}{a_J}\right]^{1/2}\cos(i) \qquad (1)$$

where a, e and i are the orbital semi-major axis, eccentricity and inclination, respectively, and $a_J = 5.2$ au is the semi-major axis of Jupiter. T_J parameterizes the relative velocity between an object and Jupiter at their closest approach, and is approximately conserved in the circular restricted three-body dynamics approximation (*Tisserand* 1896; *Murray and Dermott* 2000), even in the event of close encounters (*Carusi et al.* 1995). Jupiter itself has $T_J = 3$. Asteroids typically have $T_J > 3$ and comets have $T_J < 3$ (*Vaghi* 1973).

To make sense of the alphabet soup used to describe small solar system populations, we show in Figure 1 a simple classification scheme based on T_J and whether or not

observable mass loss exists. Within the comet population, long period comets (LPCs) have $T_J < 2$ and orbital periods $P_{\rm orb} \geq 200$ yr, Halley-type comets (HTCs) have $T_J < 2$ and $P_{\rm orb} < 200$ yr, and Jupiter-family comets (JFCs) have $2 \leq T_J \leq 3$ (*Levison* 1996). The different orbital properties of these populations reflect their origins, with LPCs supplied from the Oort Cloud, JFCs from the Kuiper belt, and HTCs from a thus far ambiguous source, with likely contributions from both the Oort cloud and the scattered disk component of the Kuiper belt (*Dones et al.* 2015, also see chapter by Kaib and Volk). Damocloids and Asteroids on Cometary Orbits (ACOs) are inactive bodies with $T_J < 2$ and $2 \leq T_J \leq 3$, respectively, paralleling the distinction between LPCs and JFCs.

In the classical view of the solar system described above, asteroids and comets formed at different temperatures in locations interior and exterior to the snow line, respectively, and have been preserved more or less in their formation locations for the past 4.5 Gyr. In principle, these different formation conditions and source regions should produce objects with distinct physical and dynamical properties. As such, small solar system objects should be uniquely classifiable into one of these categories or the other.

Recently, however, a more nuanced picture has emerged, with classical asteroids and comets now understood as simply end-members of observational, physical, and dynamical continua. A key practical problem with the observational classification of objects based only on observations of activity is that it is dependent on instrumental sensitivity (Section 2). Furthermore, we now know that many other processes besides ice sublimation can lead to visible mass loss (Section 3), meaning that activity is possible for a much
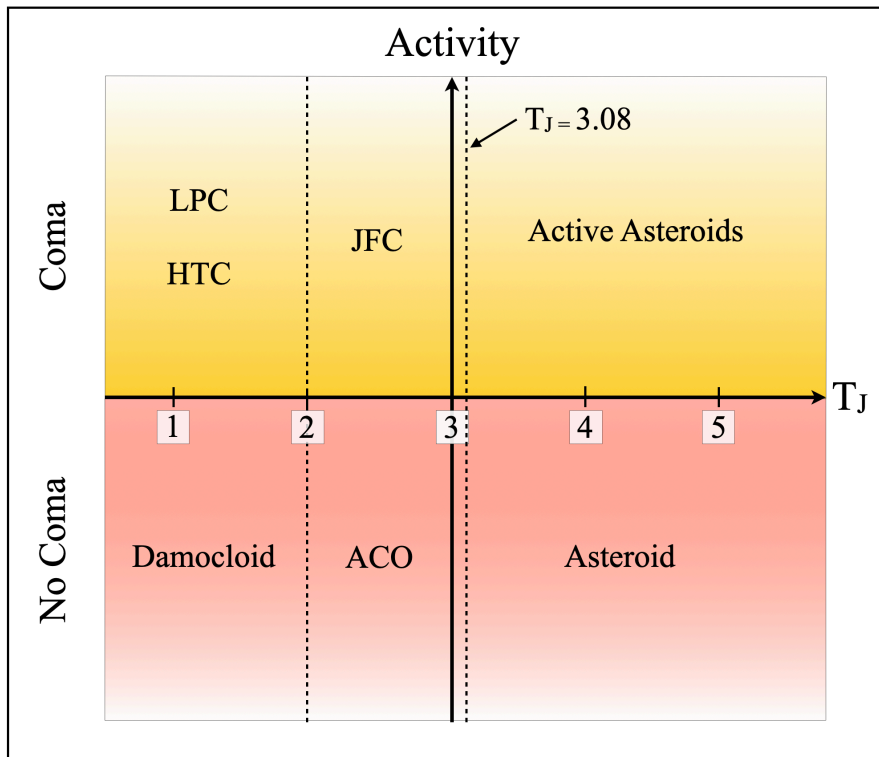

Fig. 1.— Classification diagram for small bodies discussed in this chapter, showing the Tisserand parameter with respect to Jupiter (T_J) vs. whether or not a coma has ever been detected. Acronyms are explained in Section 1. Centaurs (not shown) can appear anywhere in this plot. The vertical dashed line marked $T_J = 3.08$ denotes the nominal lower bound for active asteroids.

broader range of objects beyond just those containing ice.

We also now recognize that asteroids and comets did not originate in wholly distinct regions of the solar system, as was formerly believed (Section 4). Comets may be less volatile-rich than the half rock, half ice mixture envisioned by *Whipple* (1950), and they contain a curious combination of the most volatile ices from the outermost regions of the protoplanetary disk and high-temperature, crystalline silicates from the inner edge of the protoplanetary disk (*Westphal et al.* 2009, also see chapters by Bergin et al. and Filacchione et al.). Isotopic evidence from meteorites shows two types of material which accreted separately (perhaps interior and exterior to Jupiter's orbit, and perhaps not simultaneously), but which are now intermingled in the asteroid belt (*Warren* 2011; *Lichtenberg et al.* 2021). As we discuss later, there is clear evidence for near-surface ice in the main asteroid belt where its survival was previously thought to be implausible. Some of this mixing across the protoplanetary disk might have been forced by the radial migration of the planets, the latter identified first from the unexpectedly dense resonant populations in the Kuiper belt. The snow line itself is now understood to be a dynamic entity, which moved in response to time-dependent heating sources in the protoplanetary disk (*Harsono et al.* 2015).

Finally, dynamically, T_J is an imperfect discriminant due to its neglect of planetary perturbers other than the Sun and Jupiter and lack of consideration of nongravitational perturbations due to asymmetric outgassing. We now know that not only is the dynamical boundary between asteroids and comets better characterized as a range of T_J values rather than a sharp threshold at a single T_J value (i.e., $T_J = 3$), the boundary is also porous, with objects capable of passing through to the other side in both directions, so obscuring their true dynamical origins (Section 5).

In this chapter, we review the current state of knowledge concerning objects that sit in the ambiguous space between classical rocky asteroids and classical icy comets. We will consider objects that originate as either classical comets or classical asteroids and evolve observationally, physically, or dynamically into the other type of object, as well as objects for which having characteristics of both asteroids and comets is simply part of their intrinsic nature. While these objects have often been termed "transition objects" in earlier literature, the title of this chapter reflects the fact that not all of these objects are actually in the midst of transitioning from one type of small body to another. Instead, there is simply a broad diversity of objects that span the

range of observational, physical, and dynamical properties commonly attributed to either asteroids or comets in a continuous, rather than discrete, fashion (e.g., *Hsieh* 2017).

In addition to the topics above, we will discuss key examples of objects that have properties of both classical asteroids and comets: active asteroids (Section 6), inactive comets (Section 7), and Centaurs (Section 8). While these do not comprise an exhaustive list, they provide instructive examples relevant to the entire asteroid-comet continuum for small solar system bodies. We will then conclude with a discussion of future research prospects (Section 9).

2. ACTIVITY DETECTION

2.1. Overview

One factor in the growing recognition of asteroid-comet continuum objects is a steady improvement in the ability of astronomers to detect weak activity, enabled by the use of larger, more sensitive telescopes, and by increasing numbers of wide-field, time-resolved surveys. A second factor is the recognition that weak activity exists to be detected, which adds an equally important, albeit psychological, dimension to the growing rate with which these objects are perceived. The most direct method of activity detection is resolved imaging, which typically reveals the presence of comet-like features like comae or tails. Other methods, including photometric analysis, spectroscopic detection of gas, detection of debris streams associated with small solar system bodies, and detection of non-gravitational perturbations, can also reveal the presence of activity.

2.2. Resolved Imaging

Resolved imaging of mass loss is the gold standard and most common means by which objects are determined to be active. The optical scattering efficiency (measured as cross-section per unit mass) of dust is much larger than that of resonance fluorescence from common molecules. Therefore, direct imaging typically reveals only ejected dust, whether or not gas is present. Even in classical comets, for which we are sure that gas drag drives mass loss, gas is commonly undetectable against the continuum of sunlight scattered from dust, particularly in observations taken at heliocentric distances $r_H \gtrsim 2$ au.

For weakly active objects, direct imaging of mass loss requires sensitivity to faint near-nucleus surface brightness features and is thus a function of telescope size, angular resolution, sky brightness, and more. Most active asteroids and Centaurs have been discovered in data from wide-field surveys, for which activity detection is typically not prioritized. Unfortunately, the surface brightness detection limits of most of those surveys are not well documented, making it difficult to use their data to quantitatively characterize populations of active bodies. Two exceptions are

the wide but shallow survey of *Waszczak et al.* (2013) and the deep but narrow-field "Hawaii Trails Project", where the latter survey resulted in the discovery of a fan-like dust tail associated with 176P/LINEAR, then known as asteroid (118401) 1999 RE_{70}, with an R-band surface brightness of $\Sigma_R = 25.3$ mag arcsec^{-2} (*Hsieh* 2009). The relatively shallow depths of most wide field surveys, though, mean that low-level activity is not well constrained for the vast majority of asteroids. Many asteroids that are currently considered inactive could in fact be weakly active but have thus far escaped detection (*Sonnett et al.* 2011).

This view is anecdotally supported by the discovery of activity in (3200) Phaethon, (3552) Don Quixote, and (101955) Bennu. Phaethon (Section 6.3.5) and Don Quixote (*Mommert et al.* 2014) were only found to be active after intensive targeted observational efforts motivated by independent indicators that the objects could be active (i.e., Phaethon's association with the Geminid meteor stream and Don Quixote's dynamically cometary orbit with $T_J = 2.3$), while activity was observed unexpectedly in situ for Bennu by the visiting OSIRIS-REx spacecraft (Figure 2; Section 6.3.6).

Fig. 2.— Reverse polarity image of 0.5 km diameter asteroid (101955) Bennu from OSIRIS-REx showing a swarm of centimeter-sized particles in the upper left of the image. Image credit: NASA/Univ. of Arizona.

Identification of active objects is also complicated by the fact that activity is usually transient. Active icy objects can become dormant when their surface volatiles are depleted or buried by a non-volatile crust (*Jewitt* 1996). Additionally, even modest orbital eccentricities can strongly affect water ice sublimation rates (because sublimation is an exponential

function of temperature and hence of heliocentric distance) and therefore dust production rates. Thus, even very deep observations of main-belt objects away from perihelion do not exclude the possibility of sublimation-driven activity when closer to the Sun (e.g., *Hsieh et al.* 2015a). Meanwhile, visible mass loss caused by other processes, e.g., impacts and rotational destabilization, can be very short-lived and can occur at any time (not just near perihelion), meaning that it is almost always discovered by chance in all-sky surveys (e.g., *Birtwhistle et al.* 2010; *Larson* 2010; *Smith et al.* 2019). As such, the vast majority of such events have undoubtedly gone undetected due to the fact that we are, and will continue to be for the foreseeable future, unable to observe all small solar system bodies at all times.

2.3. Photometric Detection

Very sensitive searches for activity can be conducted by comparing measurements of the apparent magnitude, $m_\lambda(r_H, \Delta, \alpha)$, of an object in a filter with effective wavelength, λ, with predictions based on the absolute magnitude in the same filter, H_λ. The absolute magnitude is defined by

$$H_\lambda = m_\lambda(r_H, \Delta, \alpha) - 5\log_{10}(r_H\Delta) + 2.5\log_{10}(\Phi(\alpha)) \tag{2}$$

where r_H and Δ are the object's instantaneous heliocentric and geocentric distances, respectively, in au, and $0 < \Phi(\alpha) < 1$ is the phase function[2]. Photometric measurements that are brighter than would be expected from an object's absolute magnitude and rotational lightcurve amplitude would then imply the presence of unresolved ejected dust within the seeing disk of that object.

Anomalous brightening was first used to identify the activity of (2060) Chiron (*Hartmann et al.* 1990), with resolved coma directly imaged soon afterwards (*Luu and Jewitt* 1990; *Meech and Belton* 1990). Since then, photometry has been used to search for and identify activity in other objects (e.g., *Cikota et al.* 2014; *Hsieh and Sheppard* 2015). Unfortunately, absolute magnitudes for most asteroids are computed from imprecise photometric data collected by the IAU's Minor Planet Center, limiting the accuracy with which their brightnesses can be predicted at any given time. An additional limitation is imposed by the unknown rotational variability of many objects. As a result, while photometric analysis provides very clear detections of activity for bright comets already showing resolved comae and tails (e.g., Figure 7 of *Ferrín and Orofino* 2021), results are ambiguous for objects with poorly characterized nucleus properties, as is true of most asteroids. We expect that photometric activity detection will become much more effective when data from the Vera C. Rubin Observatory

(see Section 9) become available. Those data will enable both the computation of precise absolute magnitudes for large numbers of small solar system bodies and precision photometry in individual observations for activity detection.

2.4. Spectroscopic Detection

Spectroscopy is a powerful tool for studying active objects, as it is essentially the only means for acquiring unequivocal evidence of volatile sublimation and can also provide additional detail about the types of volatiles present. In practice, however, spectroscopy has so far played only a small role in the study of asteroid-comet continuum objects.

At optical wavelengths, two major limitations of spectroscopy are lack of sensitivity to the dominant volatile (water) and the strong heliocentric dependence of resonance fluorescence emission. Water has no observable bands in the optical, forcing the use of trace species (e.g., CN, which has an emission band around 3883Å) as proxies. For example, one hour of spectroscopic observations targeting CN with the Keck telescope reaches production rates $Q_{CN} \sim 10^{22}$ s^{-1} at $r_H = 1$ au, falling to $Q_{CN} \sim 10^{24}$ s^{-1} at $r_H = 3$ au (*Jewitt* 2012). The water production rate in JFCs is 400 times that of CN (*A'Hearn et al.* 1995), implying spectroscopic detection limits of $Q_{H_2O} \sim 4 \times 10^{24}$ s^{-1} (~ 0.1 kg s^{-1}) at $r_H = 1$ au but only $Q_{H_2O} \sim 4 \times 10^{26}$ s^{-1} (~ 10 kg s^{-1}) at $r_H = 3$ au. This is why JFCs and LPCs that are visibly active at ≥ 3 au and active Centaurs at much largely distances commonly show no optical evidence for gas. Worse, there is no fundamental reason why the ratio of CN to water in classical comets should be applicable to other objects like active asteroids, and in fact, reason to believe that it may be far lower (e.g., *Prialnik and Rosenberg* 2009), meaning that water production rate limits inferred from CN observations are of dubious value.

Spectroscopic observations at non-optical wavelengths are better suited to studying volatile sublimation (see chapter by Bodewits et al.) but have not been used extensively for the subjects of this chapter. One exception is the successful detection of outgassing by (1) Ceres in the form of multiple detections of the $1_{10} - 1_{01}$ ground-state transition line of ortho-water at 556.939 GHz using the *Herschel Space Observatory* (*Küppers et al.* 2014). Detections of CO rotational transitions at submillimeter and millimeter wavelengths have also been secured in comets and Centaurs at large heliocentric distances (see chapter by Fraser et al.).

2.5. Debris Stream Detection

The association between meteoroid streams and active comets has been long recognized (e.g., *Whipple* 1951). There is also a growing number of identified associations between meteoroid streams and asteroids (see *Jenniskens* 2008, 2015). The latter associations have been interpreted

---

[2]The phase function is equal to the ratio of the scattered light at phase angle α to that at $\alpha = 0°$. It is affected both by the apparent illuminated fraction of the surface and by microscopic scattering effects in the regolith.

as indicating unseen mass loss from those otherwise apparently inert bodies. Famously, the association of the Geminid meteoroid stream with Phaethon (*Gustafson* 1989; *Williams and Wu* 1993) led to the first suggestions that Phaethon was losing mass (see Section 6.3.5). Other suspected asteroidal meteor stream parents (e.g., *Ryabova* 2002; *Babadzhanov* 2003; *Babadzhanov et al.* 2015) could also be experiencing unseen mass loss (see chapter by Ye and Jenniskens). Divergence between the orbital elements of debris streams and their parents results from gravitational perturbations by the planets and, potentially, from unknown non-gravitational effects (e.g., *Kaňuchová and Neslušan* 2007).

Finally, several asteroids, notably the near-Earth asteroids (NEAs) 2201 Oljato and 138175 (2000 EE104), are associated with distinct and repeated disturbances in the magnetic field carried by the solar wind, called Interplanetary Field Enhancements (IFEs; Section 3.8), tentatively interpreted as drag from charged nanodust particles left behind along the orbits of these bodies.

2.6. Non-Gravitational Acceleration

Anisotropic mass loss from a small body creates a recoil force that can measurably perturb the orbit relative to purely gravitational motion, where non-gravitational accelerations are well-known to exist for comets (*Whipple* 1950). Sublimation-driven mass loss from a spherical nucleus of radius r_n and density ρ at rate $\dot{M}$ leads to an acceleration

$$\alpha_{ng} = \frac{3k_R V_g \dot{M}}{4\pi \rho r_n^3} \qquad (3)$$

in which V_g is the gas velocity and $k_R \sim 0.5$ is a dimensionless constant to account for the fact that the flow is neither perfectly isotropic ($k_R = 0$) nor perfectly collimated ($k_R = 1$). For illustration, for plausible values $V_g = 500$ m s^{-1}, $\rho = 500$ kg m^{-3}, and $r_n = 10^3$ m, we find $\alpha_{ng} = 10^{-10}\dot{M}$ m s^{-2}. Expressed as a fraction of the local gravitational attraction to the Sun at 3 au ($g_\odot = 7 \times 10^{-4}$ m s^{-2}), this is $\alpha_{ng}/g_\odot \sim 1.7 \times 10^{-7}\dot{M}$, which should be detectable for the best astrometrically observed asteroids for production rates of $\dot{M} \sim 1$ to 10 kg s^{-1} (*Hui and Jewitt* 2017). This method is limited in its application mainly by the reliability of astrometry, particularly when plate-era data are used to obtain long astrometric arcs.

3. ACTIVITY MECHANISMS

3.1. Overview

A variety of mechanisms in addition to sublimation can lead to observable mass loss, expanding the range of objects that we must consider to have the potential for activity. We briefly discuss the major mass loss mechanisms, which may operate alone or in conjunction.

3.2. Ice Sublimation

There is now substantial evidence that water ice is currently present (and possibly widespread) in objects with dynamically stable orbits in the main asteroid belt, and not just in objects from the outer solar system. This revelation raises the possibility of being able to conduct present-day studies of ice possibly from a part of the protosolar disk not sampled by the classical comet population, and also presents new opportunities for studies of the thermal and dynamical evolution of small bodies both in the early and present-day solar system (e.g., *Schörghofer* 2008; *DeMeo and Carry* 2014; *Hsieh and Haghighipour* 2016).

Exposed, dirty (low albedo) water ice at asteroid belt distances is quickly lost by sublimation. However, *Fanale and Salvail* (1989) noted that water ice can persist at relatively shallow depths (e.g., a few centimeters to meters) when protected by a nonvolatile surface layer. Its persistence is more likely at high latitudes on objects with larger semimajor axes, slow rotation rates, low thermal conductivity, and low obliquity. *Schörghofer* (2008) confirmed these findings, introducing the concept of a "buried snowline", i.e., the distance from the Sun beyond which subsurface ice can persist over the age of the solar system. That said, near-surface asteroid ice is likely to be dominated by water ice, given the greater thermal instability of other volatiles in the asteroid belt (*Prialnik and Rosenberg* 2009). *Schörghofer et al.* (2020) combined models of the thermal and dynamical evolution of Themis asteroid family members, finding that most of their subsurface ice would be retained even during transitions to near-Earth orbits, assuming stable spin pole orientations. This raises the intriguing possibility that asteroid ice could one day be sampled by a near-Earth mission, and reminds us that the outer asteroid belt could be a source of at least some terrestrial planet volatiles.

Buried ice can be exposed and activated by triggering events like impacts (e.g., *Haghighipour et al.* 2016), rotationally-induced landslides (e.g., *Scheeres* 2015; *Steckloff et al.* 2016), and inward drift of the perihelion distance (e.g., *Rickman et al.* 1990; *Fernández et al.* 2018). This is only possible, however, if the ice depth is shallow, because deep disturbance of the surface is unlikely. Shallow ice could exist on fragments from the catastrophic disruption of larger parent bodies, as in those that form asteroid families (see *Nesvorný et al.* 2008, 2015; *Novaković et al.* 2012). Ice-containing fragments would be more easily triggered by, for example, small impacts excavating just a few meters of the surface (*Hsieh et al.* 2018c).

Ice sublimation rates are very sensitive to temperature, such that even modest temperature differences between perihelion and aphelion give rise to substantial variations in activity strength, and therefore detectability. Neglecting a small term due to conduction, the energy balance equation
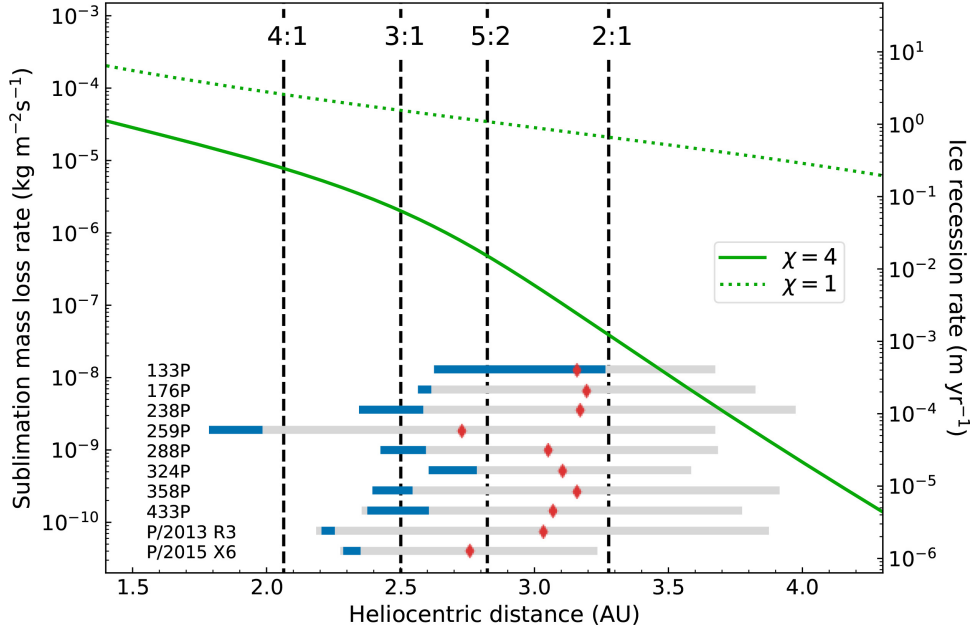
Fig. 3.— Plot of mass loss rates due to water sublimation from a sublimating gray body and ice recession rates per year as functions of heliocentric distance over the range of the main asteroid belt using the isothermal approximation ($\chi = 4$; solid curved green line) and subsolar approximation ($\chi = 1$; dotted green line). The positions of the 4:1, 3:1, 5:2, and 2:1 mean-motion resonances with Jupiter are marked with vertical dashed black lines. Also plotted are horizontal light gray bars showing the full heliocentric ranges of a selection of main belt comet (MBC) orbits (see Section 6.2) with overlaid blue bars showing the heliocentric range over which activity was detected for those MBCs, and red diamonds indicating each MBC's semimajor axis distance. After *Hsieh et al.* (2015a)

.

at the surface of a sublimating gray body may be written

$$\frac{F_{\odot}}{r_H^2}(1 - A) = \chi \left[\varepsilon \sigma T^4 + L f_D \dot{m}_w(T) \right] \quad (4)$$

where T is the equilibrium surface temperature of the body, $F_{\odot} = 1360$ W m^{-2} is the solar constant, heliocentric distance r_H is in au, $A = 0.05$ is the assumed Bond albedo, the distribution of solar heating is parameterized by χ, σ is the Stefan-Boltzmann constant, $\varepsilon = 0.9$ is the assumed effective infrared emissivity, $L = 2.83$ MJ kg^{-1} is the (nearly temperature-independent) latent heat of sublimation of water ice, f_D represents the reduction in sublimation efficiency caused by a growing rubble mantle, where $f_D = 1$ in the absence of a mantle, and $\dot{m}_w$ is the water mass loss rate due to sublimation. In this equation, $\chi = 1$ applies to a flat slab facing the Sun at all times, known as the subsolar approximation, and produces the maximum attainable temperature, while $\chi = 4$ applies to an isothermal surface (e.g., for a fast-rotating body or low thermal inertia), and corresponds to the minimum expected temperature.

The sublimation rate of ice into a vacuum is given by

$$\dot{m}_w = P_v(T) \left(\frac{\mu m_H}{2\pi k T} \right)^{1/2} \quad (5)$$

where $m_H = 1.67 \times 10^{-27}$ kg is the mass of the hydrogen

atom, $\mu = 18$ is the molecular weight of water, and k is the Boltzmann constant. The corresponding ice recession rate, $\dot{\ell}_i$, is given by $\dot{\ell}_i = \dot{m}_w/\rho$, for an object with a bulk density ρ. The temperature-dependent sublimation pressure, $P(T)$, is obtained from the Clausius-Clapeyron relation, or from experimental data. Solving Equations 4 and 5 iteratively gives the equilibrium temperature and the sublimation rate of a sublimating gray-body at a given heliocentric distance.

Expected water sublimation rates computed using the equations above, assuming $f_D = 1$, for the extreme subsolar and isothermal approximations are plotted in Figure 3. We see from the figure that even objects whose orbits keep them entirely confined to the main asteroid belt have expected water sublimation rates that can vary by several orders of magnitude from aphelion to perihelion. For main-belt objects that are only weakly active near perihelion, despite their modest eccentricities, it is therefore entirely plausible for sublimation in these objects to be detectably strong near perihelion and undetectably weak near aphelion, just like classical comets with much larger perihelion-to-aphelion heliocentric distance excursions.

Observationally, the expected characteristics of sublimation-driven activity include long-duration mass loss and recurrent activity (e.g., *Hsieh et al.* 2012a). Unlike mass loss
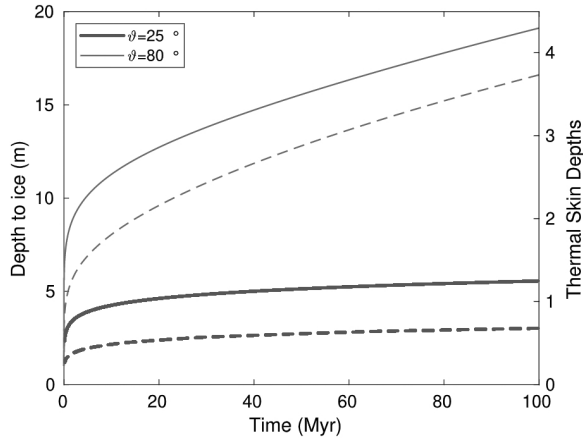
Fig. 4.— Plot of depth to ice in a thermal model as a function of time for a main-belt asteroid in a stationary orbit with $a = 3$ au and $e = 0$ for obliquities of $\vartheta = 25°$ (lower set of curves) and $\vartheta = 80°$ (upper set of curves). The assumed thermal diffusivity is $\kappa = 3.8\times10^{-7}$ m^2 s^{-1}. Within the first thermal skin depth, ice retreat is rapid, but total retreat is small for $\vartheta = 25°$, even after 100 Myr. Solid lines mark ice evolution using uniform thermal properties for all regolith, while dashed lines mark ice evolution using different thermal properties for ice-free and ice-rich regolith. From *Schörghofer et al.* (2020)

produced by impulsive events like impacts (Section 3.3), sublimation-driven activity is expected to persist as long as an object is warm enough for sublimation to occur and volatile material remains. Determining the duration of emission events often requires the use of numerical dust models, however, which are typically under-constrained by observations. Recurrent activity correlated with perihelion strongly suggests thermal modulation of the mass loss process, which is a natural characteristic of volatile sublimation. Other mechanisms require more contrived conditions to produce similar behavior (e.g., *Hsieh et al.* 2004), leading us to consider recurrent mass loss near perihelion to be the most dependable indicator of sublimation-driven activity currently available using remote observations.

3.3. Impacts

Images of asteroids from spacecraft reveal cratered landscapes that record a violent collisional past. Observations of the consequences of impacts can place important constraints on the material properties and internal structure of the bodies that experienced those impacts, motivating decades of crater studies (*Marchi et al.* 2015), theoretical modeling (*Jutzi et al.* 2015) and impact experiments in laboratory settings (e.g., *Housen et al.* 2018), while impacts can also excavate subsurface material which can then be directly studied. Excitingly, impact experiments on real-world solar system bodies (e.g., *A'Hearn et al.* 2005; *Schultz et al.*

2010; *Saiki et al.* 2017) as well as studies of natural impact events occurring in real time (see Section 6.3.2) have also recently become possible. The velocity dispersion in the asteroid belt is $\sim$5 km s^{-1}, resulting in intermittent asteroid-asteroid collisions that are highly erosive or, if sufficiently energetic, destructive. Collisions also occur at the smallest scales, leading to steady erosion by micrometeoroids. Although small and large impacts are part of a continuum, it is useful to describe these extremes separately.

3.3.1. Micrometeoroid Erosion

Micrometeoroid impacts set an absolute lower limit to the rate of steady mass loss from a body. Few impacting particles can penetrate deeply because of the steep size and energy distributions of projectiles, and so the erosion is fastest at the surface. On the Moon, where the gravity is non-negligible ($g_{\leftmoon} = 1.6$ m s^{-2}), micrometeoroid impact-produced fragments are recaptured, forming a regolith that is overturned or "gardened" by continued impacts. Measurements of the lunar gardening rate show that the top 1 m of the regolith is over-turned in about 10^9 yr while the top 1 cm is mixed in only 10^6 yr (*Arvidson et al.* 1975; *Heiken et al.* 1991; *Horz and Cintala* 1997). To set a crude upper limit to asteroid erosion, we assume that the material that is gardened on the Moon would instead be launched above escape speed and lost from a km-sized (low gravity) asteroid, and that the impact rates on the Moon and in the asteroid belt are comparable. We take the higher lunar value, $dr/dt = 10^{-8}$ m yr^{-1}, as a representative rate of loss. With $\rho = 10^3$ kg m^{-3}, the micrometeorite erosion mass flux is $\mathcal{L} = \rho\,dr/dt \sim 10^{-5}$ kg m^{-2} yr^{-1}.

Sandblasting by micrometeorites, at a rate given by $\dot{M}_\mu = 4\pi r_n^2 \mathcal{L}$ for a spherical body of radius r_n, is evidently very slow. Expressing r_n in km, we obtain

$$\dot{M}_\mu = 4 \times 10^{-6} r_n^2 \text{ kg s}^{-1}. \qquad (6)$$

A r_n=1 m boulder would have a $\sim$3$\times$10^7 yr lifetime against micrometeoroid erosion, while a r_n=1 km body would lose $\sim$4$\times$10^{-6} kg s^{-1}, and could do so indefinitely. Other than for 0.25 km radius Bennu, whose $\sim 10^{-7}$ kg s^{-1} mass loss rate (*Hergenrother et al.* 2020) is $\sim$0.4$\dot{M}_\mu$, all remote detections of asteroid, comet, and Centaur activity have thus far exceeded $\dot{M}_\mu$ by 3 to 10 orders of magnitude.

3.3.2. Macroscopic Impacts

Most of the mass and available impact energy in the asteroid population is carried by the largest projectiles, but large bodies and impacts are rare and their effects are transient. Nevertheless, individual large impactors are easily capable of generating observable quantities of dust. Several impact events have been detected in the main asteroid belt within the last decade. The best example of impact destruction of an asteroid is provided by the 100 m scale

354P/LINEAR (Section 6.3.2; *Jewitt et al.* 2010a; *Snodgrass et al.* 2010; *Kim et al.* 2017a). P/2016 G1 may also be a collisionally disrupted asteroid of similar scale (*Moreno et al.* 2016b). Similar collisions must also occur in the Kuiper belt but have yet to be observed.

Figure 5 shows the timescale for the impact destruction of a given main-belt asteroid as a function of its diameter, D, where we see that a $D = 1$ km asteroid has a collisional lifetime ~ 0.4 Gyr, decreasing to ~ 60 Myr for $D = 0.1$ km. Asteroids larger than $D \sim 10$ km, on average, should survive against collisions over the 4.5 Gyr age of the solar system. The likelihood of witnessing a destructive collision on any *specific* asteroid in a human lifetime is therefore negligibly small. However, the likelihood of observing a collisional destruction *somewhere* in the asteroid belt, when integrated over the asteroid size distribution, is much higher (Figure 6). Specifically, τ_{CD} (yr), the interval between successive destructions averaged over the whole main belt is well represented by

$$\log_{10} \tau_{CD} = 2.62 + 2.88 \log_{10} D. \tag{7}$$

for D in km (see Figure 6). Equation 7 gives $\tau_{CD} \sim 400$ yr for $D = 1$ km, falling to $\tau_{CD} \sim 1$ yr for $D = 0.1$ km and $\tau_{CD} \sim 30$ s (!) for $D = 1$ m. Independent modeling of survey data suggests that up to 10 catastrophic disruption events brighter than $V = 18.5$ mag may be discoverable each year by current and future asteroid surveys (*Denneau et al.* 2015).

Fig. 6.— Interval between collisional disruptions as a function of asteroid diameter, integrated over the asteroid size distribution. Adapted from *Bottke et al.* (2005)

Compared to catastrophic collisions, collisions resulting in less than complete destruction, so-called "cratering collisions", should be more common. The minimum size of cratering impact that gives rise to an observable signature is poorly modeled, being a function of many uncertain parameters (e.g., *McLoughlin et al.* 2015). For example, the mass and size distribution of ejecta determine the peak brightness and persistence time (because particles are cleared by solar radiation pressure, which acts in inverse proportion to the particle size). Given better collision rate determinations, we should be able to map the spatial distribution of small (m-scale) impactors through the asteroid belt.

A cratering impact between a 20 m to 40 m scale projectile and the 113 km diameter asteroid (596) Scheila (see section 6.3.2) was a one in $\sim 10^4$ year event for this object but, given that there are of order 200 asteroids of similar or larger size, should occur once every ~ 50 years somewhere in the asteroid belt (*Jewitt* 2012). As monitoring of the sky improves, we should soon be able to detect cratering collisions throughout the asteroid belt in great abundance (see Section 9).

3.4. Rotational Destabilization

Rotational instability causes mass loss when the centrifugal forces exceed the sum of gravitational and cohesive forces acting towards the center of mass. Like impact disruptions (Section 3.3), rotational disruptions can place important constraints on a body's interior properties (e.g., *Hirabayashi et al.* 2015). For a strengthless $a \times b \times c$ el-
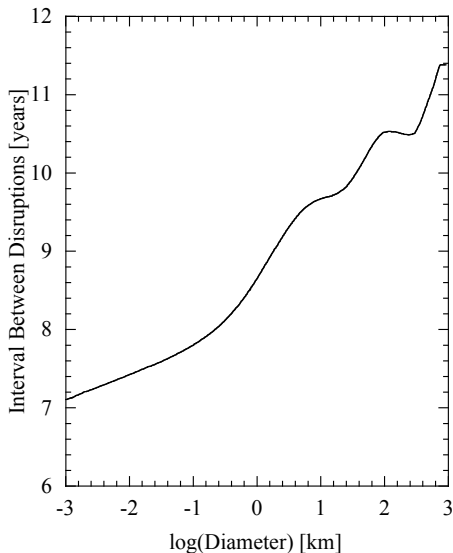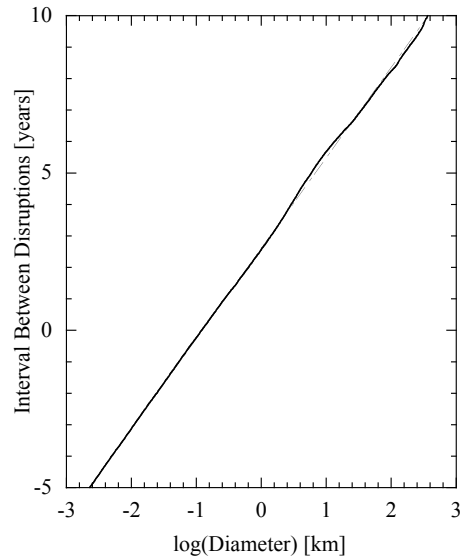

Fig. 5.— Interval between collisional disruptions of main-belt asteroids as a function of their diameter in the range 1 m to 1000 km. Adapted from *Bottke et al.* (2005).

lipsoid, with $a = b \leq c$, bulk density ρ, and rotation about a minor (minimum energy, maximum moment of inertia) axis, the critical, size-independent rotation period is

$$P_c = \left(\frac{3\pi}{G\rho}\right)^{1/2}\left(\frac{c}{a}\right) \qquad (8)$$

where $G = 6.67 \times 10^{-11}$ N kg^{-2} m^2 is the gravitational constant. For a sphere, $c/a = 1$, with $\rho = 10^3$ kg m^{-3}, we find $P_c = 3.3$ hours. This rises to $P_c = 4.0$ hours for a body with $c/a = 1.2$ (the modal axis ratio of small asteroids from *Szabó and Kiss* 2008), with the instability occurring at the tips of the ellipsoid. Several active asteroids rotate with periods comparable to P_c (c.f. Table 1), raising the possibility that rotational instability plays a role in the ejection of material from those objects.

A complicating factor in the application of Equation 8 is that even very modest values of material cohesion (used here to mean any combination of tensile strength and shear strength) can hold together a rotating asteroid. To see this, we use the rotational energy density in a uniform sphere as an estimate of the average rotational stress, S_0, obtaining

$$S_0 \sim \rho V_{eq}^2, \qquad (9)$$

where $V_{eq} = 2\pi r/P_c$ is the equatorial velocity. With the above parameters and $r = 1$ km, we find $S_0 \sim 280$ N m^{-2}, which is easily overcome by material cohesion. Most asteroids and comets likely possess a weak, rubble-pile structure in which gravity, rotation and van der Waals forces all play a role. The magnitude of the latter is $\sim S_0$ (*Scheeres et al.* 2010; *Sánchez and Scheeres* 2014; *Sánchez et al.* 2021), meaning that cohesion can nevertheless substantially control a body's mass loss and shape. Bodies with a weakly cohesive regolith are subject to mass movement and, eventually, mass shedding as particulate material escapes from the equator. Evidence for this process is compelling in "top-shaped" asteroids (Figure 7), whose shapes are formed by skirts of material that has migrated from higher latitudes towards the equator (*Harris et al.* 2009).

The spin of an inert body can change because of radiative torques (e.g., the Yarkovsky–O'Keefe–Radzievskii–Paddack, or YORP, effect; *Bottke et al.* 2006), torques from outgassing if volatiles are present (*Jewitt* 2021), and impacts (*Marzari et al.* 2011). Eight asteroids in the published literature display evidence for spin-up, namely (1620) Geographos (which interestingly is also a suspected meteor stream parent; *Ryabova* 2002, also see Section 2.5), (1862) Apollo, (3103) Eger, (25143) Itokawa, (54509) YORP, and (161989) Cacus, (1685) Toro, and (10115) 1992 SK (*Rozitis and Green* 2013; *Lowry et al.* 2014; *Durech et al.* 2018, 2022). Figure 8 shows characteristic spin-up timescales for these asteroids computed using $\tau = \omega/\dot{\omega}$, where ω is the measured angular frequency, as a function of diameter, where the 10 m scale asteroid 2012 TC$_4$ shows evidence for multiple periods and spin-up (*Lee et al.* 2021) but is
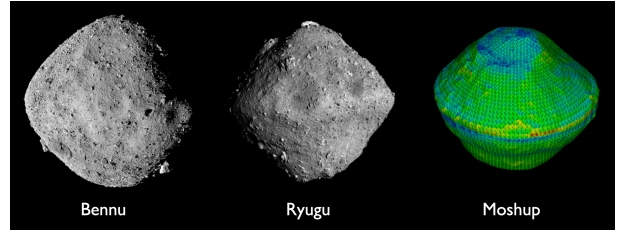

Fig. 7.— Three examples of rotationally-shaped asteroids with equatorial skirts. (101955) Bennu, (162173) Ryugu and (66391) Moshup have diameters 500 m, 900 m and 1300 m, respectively. Bennu and Ryugu were imaged by spacecraft, while the Moshup image was derived from radar observations. Image credits: NASA/Goddard/Univ. of Arizona (Bennu); JAXA, Univ. of Tokyo, and collaborators (Ryugu); *Ostro et al.* (2006) (Moshup).

not plotted here. Uncertainties for τ_Y are dependent on uncertainties for the albedo, size, shape, density and thermal properties of the measured asteroids. For illustration, we show error bars indicating $\pm 50\%$ uncertainties.
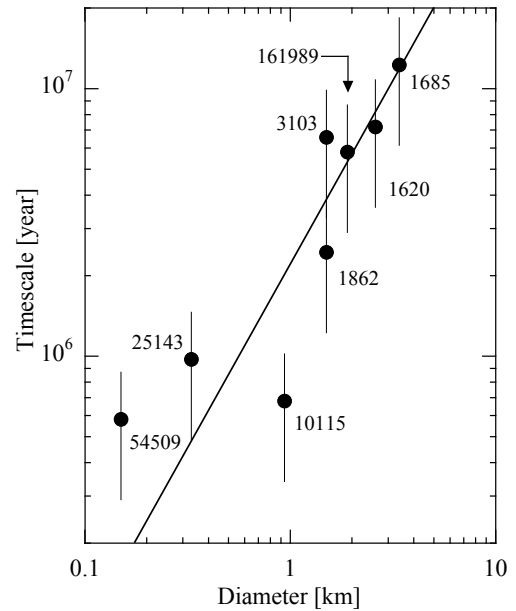

Fig. 8.— Empirical YORP timescales for small asteroids (marked by their numerical designations) as a function of diameter, using published measurements of spin-period changes. The plotted objects have semimajor axes $a = 1.0$ to 1.5 au, and the plotted line is given by Equation 10.

The timescale for spin-up by YORP torque, τ_Y, is expected to vary as $\tau_Y = \Gamma a_{au}^2 D^2$, where Γ is a constant, a_{au} is the semimajor axis in au, and D is the effective diame-

ter. The a_{au}^2 dependence results from the fading of sunlight described by the inverse square law. The D^2 dependence arises because the timescale is given by the ratio of the moment of inertia (which varies as D^5) to the torque (given by the product of the surface area and the moment arm for the torque, together $\propto D^3$). The constant, Γ, must be determined empirically, since it is dependent on many unknown details of each asteroid. Under the assumption that the spin-up of objects in Figure 8 is due to YORP, we compute a least-squares fit for the YORP timescale given by

$$\tau_Y = (1.4 \pm 0.3) \times 10^6 a_{au}^2 D^{1.4 \pm 0.3} \qquad (10)$$

which is shown in the figure as a solid line. The best-fit index, $g = 1.4 \pm 0.3$, is consistent with the expected value of $g = 2$ to within two standard deviations[3]. If we instead force a D^2 dependence, a fit to the data gives $\tau_Y = (0.7 \pm 0.1) \times 10^6 a_{au}^2 D^2$. Both fits (as well as Figure 8) indicate that a 1 km diameter object located at $a_{au} = 3$ au should have a characteristic spin-up time from $\tau_Y \sim 6$ to 13 Myr, with a considerable scatter due to intrinsic differences (in shape, roughness, thermal diffusivity, spin vector magnitude and direction) between the asteroids. We take $\tau_Y = 10$ Myr at $a_{au} = 3$ au as a middle value. This is much shorter than the ~ 0.4 Gyr collisional lifetime of a 1 km diameter main-belt asteroid (*Bottke et al.* 2005), showing the potential importance of rotational breakup in weak asteroids. If sublimating volatiles are present, equally rapid spin-up can be achieved by tiny (e.g. 10^{-3} kg s^{-1}) mass loss rates, provided they are sustained over long times (*Jewitt* 2021).

A major unknown in Figure 8 and Equation 10 concerns the long-term stability of the applied torque. Models show that even very small changes in surface topography can result in significant changes in the magnitude and even direction of the YORP torque (e.g., *Statler* 2009). Topographical changes can result from YORP itself (leading to feedback in which the change in shape caused by the equatorward movement of material can alter the body shape and YORP torque that caused the movement), or from cratering by impacts. As a result, instead of driving inexorably towards breakup, asteroids more likely migrate erratically towards it. For example, the "top-shaped" objects in Figure 7 are not necessarily all rotating near break-up; the periods of Bennu, Ryugu, and (66391) Moshup are 4.3, 7.6 and 2.8 hours, respectively. This scatter reflects the temporal instability of the YORP torque and, perhaps, the past loss of angular momentum and subsequent de-spinning by mass redistribution or shedding in these objects.

The stochastic effects of impacts can rival torques due to YORP for bodies in the size range of interest here (*Wiegert*

2015). In impact spin-up, the dominant effects are from the small number of the largest projectiles (*Holsapple and Housen* 2019). In the limiting case, an asteroid can be impact-disrupted, forming an unstable disk from which the asteroid re-accretes mass and angular momentum. Re-assembly after impact is still capable of producing top-shaped bodies like Bennu and Ryugu (*Michel et al.* 2020).

3.5. Radiation Pressure Sweeping

Solar radiation can facilitate mass loss in two ways: via direct radiation pressure and thermal radiation pressure. In the first case, a dust grain detached from the surface of a spherical asteroid of mass M_n and radius r_n feels both a gravitational attraction, $g = GM_n/r_n^2$, towards the asteroid and an acceleration away from the Sun, α, caused by solar radiation pressure. We write $\alpha = \beta g_\odot$, where $g_\odot = GM_\odot/r_H^2$ is the gravitational acceleration to the Sun, whose mass is $M_\odot = 2 \times 10^{30}$ kg, and β is the dimensionless radiation pressure efficiency of a particle of radius a. For dielectric spheres, $\beta \sim a_{\mu m}^{-1}$, where $a_{\mu m}$ is the particle radius in units of microns. Whereas g is independent of r_H, α varies as r_H^{-2}, meaning that small asteroids close to the Sun are most susceptible to dust loss from radiation pressure sweeping. For a spherical asteroid of density ρ, $\alpha/g > 1$ is satisfied when

$$a_{\mu m} < \frac{3M_\odot}{4\pi \rho r_n r_H^2} \qquad (11)$$

(*Jewitt* 2012). Equivalently,

$$a_{\mu m} \lesssim 10 \left(\frac{1 \text{ km}}{r_n}\right) \left(\frac{1 \text{ au}}{r_H}\right)^2. \qquad (12)$$

At 3 au, a km-sized asteroid can only lose sub-μm grains but on Phaethon ($r_n = 3$ km) at perihelion ($r_H = 0.14$ au), for example, particles up to $a_{\mu m} \sim 170$ μm can be swept away. This is only possible, however, for particles which are both detached from the asteroid by another process (i.e., not subject to cohesive forces binding them to the surface) and near the illuminated limb (otherwise the radiation pressure accelerates the particles downwards into the surface). Meanwhile, sunlight absorbed and thermally re-radiated has the same effect as direct radiation pressure, but with the advantage that thermal radiation is always directed outwards and so dust can be expelled from the entire dayside of the asteroid (*Bach and Ishiguro* 2021).

Neither direct nor thermal radiation pressure can detach small dust particles held to an asteroid surface by contact forces. Once these are broken, however, by sublimation drag, thermal fracture, or other processes, radiation pressure acceleration provides a mechanism to remove that dust. As such, while there are currently no known active objects for which radiation pressure sweeping is considered a dominant driver of activity, it is possible that either direct or thermal radiation pressure may serve to enhance the dust

---

[3]The small difference, if real, could result from observational selection against the detection of small asteroids with short spin-up timescales. Such objects are more likely to have been spun-up to destruction and will not survive to be measured

ejection efficacy of other mechanisms.

3.6. Electrostatic ejection

Solid surfaces exposed to solar UV photons become photoionized, with the loss of electrons resulting in a net positive sunlit surface charge (e.g., *Criswell* 1973). Meanwhile, photoelectrons re-impacting the surface concentrate in shadowed regions. As a result, spatial gradients in illumination of a surface, for example at the terminator or between the sunlit side of a particle and its shadow, produce local electric fields. These fields are capable of moving regolith dust particles, provided that inter-particle cohesive forces can be overcome. This has been known since the Lunar Surveyor missions of the mid-1960s, when unexpected horizon glow was detected after sunset and interpreted as forward scattering from $\sim$10 μm sized regolith particles at heights of $h \lesssim 1$ m above the lunar surface (*Criswell and De* 1977). To reach h requires an ejection speed $V = (2g_{\leftmoon} h)^{1/2} \sim 1.8$ m s^{-1}, where $g_{\leftmoon} = 1.6$ m s^{-2} is lunar surface gravity. In turn, V is comparable to the gravitational escape speed from a km-sized body, meaning that electrostatic ejection is a possible mechanism behind activity in asteroids (*Jewitt* 2012). Spacecraft-imaged dust "ponds" settled in local gravitational potential minima on the 17 km diameter asteroid (433) Eros provide additional evidence for the mobility of surface dust, likely influenced by electrostatic forces (*Colwell et al.* 2005).

The physics of electrostatic launch is complicated and still under investigation, particularly concerning the question of how electrostatic repulsion can overcome attractive van der Waals contact forces that bind small particles together. One recent finding is that dust ejection can occur because of the development of small scale, but extremely large (10^5 to 10^6 V m^{-1}), electric fields in cavities between grains in a porous regolith. This is the so-called "patched charge" model (*Wang et al.* 2016; *Hood et al.* 2022). Experiments show that particles up to 10 to 20 μm can be ejected at m s^{-1} speeds.

Unlike on the Moon, where electrostatically launched particles are pulled back by gravity, dust is easily lost from small asteroids so that surface charging constitutes a net loss of surface fines. *Criswell* (1973) estimated the overturning or "churn rate" of lunar dust due to electrostatic levitation to be $C = 0.1$ kg m^{-2} yr^{-1}. We estimate an upper limit to electrostatic dust losses by assuming that, on a small asteroid, all this churned material will be lost, at a rate $\dot{M} \sim 4\pi r_n^2 C$. Substitution gives $\dot{M} \sim 0.04$ kg s^{-1}. This value is small compared to the ~ 1 kg s^{-1} rates inferred in the active asteroids, but large enough to be telescopically detectable under ideal circumstances. However, this estimate is an upper limit both because not all ejected particles will be lost, and because electrostatic churning is spatially localized near shadow boundaries, not global, on the Moon.

The fundamental problem for electrostatic ejection from asteroids, however, is that $C \gg \mathcal{L}$, where $\mathcal{L}$ is the rate of production of fresh particles by micrometeoroid impact (Section 3.3.1). With no adequate source of replenishment, detachable surface dust on a small asteroid would be quickly depleted. An additional concern is that electrostatic charging is a very general process, dependent only on the presence of ionizing radiation and dust. If electrostatic losses are important, why would only some km-sized asteroids be active rather than all of them? For these reasons, electrostatic loss seems unlikely to be a major contributor to activity on most solar system bodies.

3.7. Thermal fracture

Thermal fatigue, defined as weakening of a material through the application of a cyclic temperature-related stress, has been suggested as a driver of the particle loss from Phaethon and Bennu (Sections 6.3.5 and 6.3.6). The fractional expansion resulting from a temperature change ΔT is $\alpha \Delta T$, where an expansivity of $\alpha \sim 10^{-5}$ K^{-1} is typical (*Konietzky and Wang* 1992). The resulting strain is $S \sim \alpha Y \Delta T$, where Y is Young's modulus and a multiplier of order unity, called Poisson's Ratio, is ignored. Y values for rock are very large (e.g. 10^{10} N m^{-2} to 10^{11} N m^{-2}) meaning that huge stresses of $S \sim 10^5 \Delta T$ to $10^6 \Delta T$ (N m^{-2}) can result from modest temperature excursions. For example, diurnal temperature variations $\Delta T \sim 10^2$ K, common on airless bodies, can generate estimated stresses of $S \sim 10^7$ to 10^8 N m^{-2}. Since rocks are especially weak in tension (e.g. the tensile strength of basalt is only $\sim 4 \times 10^6$ N m^{-2}), thermal fracture is expected to be an important erosive process in space, even at asteroid belt distances and temperatures (*Molaro et al.* 2015).

In a homogeneous material, the temperature gradients and resulting thermal stresses are largest on length scales comparable to the thermal skin depth, $\ell_D \sim (\kappa P)^{1/2}$, where κ is the thermal diffusivity and P is the timescale for the insolation. By substitution, the skin depth for a solid rock asteroid ($\kappa = 10^{-6}$ m^2 s^{-1}) with a rotational period of $P = 5$ hours is $\ell_D \sim 10$ cm. Boulders of size $\ell \gg \ell_D$ can be progressively fractured into smaller rocks but particles with $\ell \ll \ell_D$ will be nearly isothermal and thus less susceptible to cracking. As a result, the breakdown of rocks by thermal fracture should progressively modify the size distribution of particles in an asteroid regolith relative to the power-law distribution produced by impact fragmentation. A separate effect arises because many rocks are built from mm-sized mineral grains having different compositions and expansivities. Differential expansion between the grains naturally causes weakening and disintegration down to mm scales. On Earth, the effects of thermal fracture are amplified by the intervention of liquid water followed by freeze-thaw cracking (*Eppes et al.* 2016). On asteroids,

where there is no liquid water, thermal fracture must be less effective. Still, boulders on asteroids, for example, are often surrounded by skirts of debris likely produced by thermal cracking from the day-night temperature cycle.

Separately, the thermal unbinding of water from hydrated minerals (e.g., hydrous phyllosilicates like serpentine, brucite, muscovite, and talc) causes shrinkage and is another process capable of cracking rocks and producing dust (as in dusty, dry mud lake beds on Earth). The activation energies for dehydration of some minerals correspond to temperatures of $T \sim 10^3$ K (*Bose and Ganguly* 1994), as reached by (3200) Phaethon and other small perihelion objects. While Phaethon shows no evidence for hydrated minerals, it is not clear if this because they have already been lost or were never present (*Takir et al.* 2020). Already suspected in Phaethon, thermal destruction may play an important role in the reported depletion of low-perihelion asteroids (*Granvik et al.* 2016).
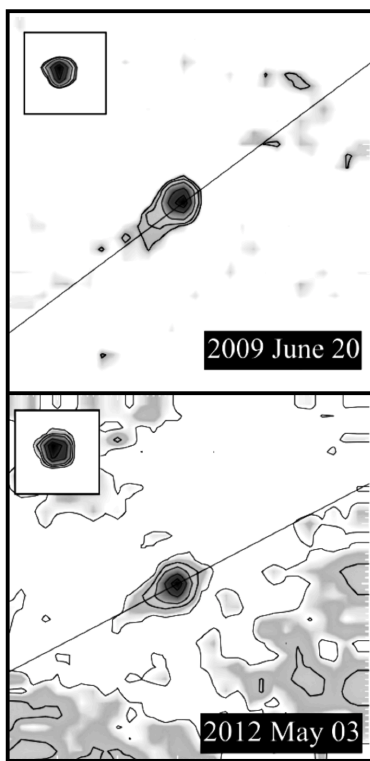

Fig. 9.— Contoured STEREO images of (3200) Phaethon against the bright background of the solar corona at perihelion in 2009 and 2012, from *Jewitt et al.* (2013b) showing its faint tail. Inset boxes showing contoured point sources are ∼8′ square, corresponding to 350,000 km at Phaethon. Straight lines show the projected Sun-Phaethon line.

In order to produce measurable activity as seen in the active asteroids, however, particles produced by thermal fracture must achieve escape velocity. Order of magnitude considerations show that m s^{-1} speeds can be generated in 10 μm-sized fragments (*Jewitt* 2012), sufficient to escape from the gravitational fields of 1 km asteroids, although larger particles will be too slow to escape. In such cases, additional forces, notably radiation pressure sweeping, might combine with thermal fracture to accelerate fresh fragments above the escape speed. Without a removal mechanism, the surface layers of an asteroid would eventually clog with small particles that could not be further fractured.

3.8. Interplanetary Field Enhancements

Several NEAs (e.g. (2201) Oljato and (138175) 2000 EE$_{104}$) are associated with distinct and repeated disturbances in the magnetic field carried by the solar wind, called Interplanetary Field Enhancements (IFEs). These disturbances, detected by spacecraft crossing the orbits of the asteroids, can last from minutes to hours and have profiles distinct from magnetic structures emanating from active regions in the Sun (*Russell et al.* 1984; *Lai et al.* 2017).

The suggested mechanism underlying IFEs is the impact ejection of nano-dust, which quickly becomes photoelectrically charged and then loads the passing solar wind, causing a magnetic field disturbance (*Russell et al.* 1984; *Lai et al.* 2017). While nano-dust itself is not optically detectable because the scattering efficiency of nano-particles is negligible, impacts should eject particles with a range of sizes, some of which should be optically detectable. A targeted search for such particles at (138175) 2000 EE$_{104}$ detected none, however, setting limits to the optical depth $\tau \lesssim 2 \times 10^{-9}$ (*Jewitt* 2020), comparable to faint JFC trails (*Ishiguro et al.* 2009).

Furthermore, the production of sufficient masses of nano-dust by impact is problematic (*Jewitt* 2020). *Lai et al.* (2017) estimated that a mass of $M_0 = 10^5$ to 10^6 kg of nano-dust would be needed to produce a single IFE. Given a range of normal (top-heavy) ejecta power-law size distributions in which most of the mass is contained in the largest particles, nano-dust constitutes only $f \sim 10^{-3.8}$ to $10^{-5.5}$ of the total mass. Therefore, to supply M_0 requires implausible source masses of $M = M_0/f \sim 10^{8.8}$ kg to $10^{11.5}$ kg, rivalling the $\sim 10^{11}$ kg mass of (138175) itself. Moreover, the planet-crossing asteroid population is comparatively rarefied, and the collision rate for such objects is likely too small to supply IFEs at the measured rate.

While no other explanations have been suggested to date, IFEs appear to be real. If they are caused by charged dust loading of the solar wind, then a solution for the mass problem and a non-impact mechanism for the production of this dust remain to be found. We know from comet 1P/Halley that nano-dust, perhaps produced by the spontaneous fragmentation of larger particles dragged out of the nucleus by gas, can be abundant in comets (*Mann* 2017). Indeed, IFE-

like magnetic field disturbances have been detected along the orbit of comet 122P/de Vico (*Jones et al.* 2003).

4. DISTRIBUTION OF VOLATILE MATERIAL

In the classical view, icy objects formed beyond the water snow line, which is the heliocentric distance beyond which temperatures are low enough for ice grains to form and become incorporated into growing planetesimals. Water interior to that distance remained in vapor form and was incorporated into forming planetesimals at a far lower rate (e.g., *Encrenaz* 2008). Icy bodies are preserved in the Kuiper belt and Oort cloud reservoirs, from which all ice-rich comets were initially believed to originate (e.g., *Duncan* 2008; *Dones et al.* 2015). Meanwhile, the inactive nature of asteroids in the inner solar system was historically interpreted to indicate a lack of ice, either because they did not accrete much icy material to begin with, or because any such material has been lost in the heat of the Sun over the age of the solar system.

Initial interpretations of the distribution of asteroid taxonomic types in the asteroid belt placed the water snow line in our solar system at ∼2.5 au (e.g., *Gradie and Tedesco* 1982; *Jones et al.* 1990), but the migratory nature of the snow line due to changing protoplanetary disk conditions (e.g., *Martin and Livio* 2012) means that icy material could have accreted throughout the asteroid belt. Moreover, icy objects from the outer solar system, well beyond any plausible location of the snow line, could have been emplaced in the inner solar system after their accretion. Evidence for this has been discovered in the isotopic compositions of meteorites, which fall into two groups identified with accretion in spatially (and, perhaps, temporally) distinct hot and cold reservoirs (*Warren* 2011). Other observational studies have revealed the otherwise unexpected presence of objects in the main asteroid belt with D-type taxonomic classifications more commonly associated with outer solar system objects (e.g., *DeMeo et al.* 2014; *Hasegawa et al.* 2021a). Numerical models also suggest that small bodies from the outer solar system could have been scattered inward as a consequence of giant planet migration early in the solar system's history (*Levison et al.* 2009; *Walsh et al.* 2011), or perhaps even as a consequence of giant planet formation itself (*Raymond and Izidoro* 2017).

In addition to finding that some inner solar system objects may contain more ice than typically assumed, recent work has also demonstrated that some outer solar system objects may also contain less ice than typically assumed. Dynamical models of early solar system evolution, both including and excluding planetary migration, predict that some objects originally formed in the terrestrial planet region could have been ejected from the inner solar system, resulting in a small fraction of planetesimals that are predominantly rocky currently residing in the Oort Cloud

(*Weissman and Levison* 1997; *Walsh et al.* 2011; *Izidoro et al.* 2013; *Shannon et al.* 2015). When perturbed into the inner solar system, these objects would then be identifiable as possessing orbits characteristic of long-period comets, while also being nearly or completely inert (e.g., *Weissman and Levison* 1997; *Meech et al.* 2016; *Piro et al.* 2021).

5. DYNAMICS

As mentioned in Section 1, the canonical $T_J = 3$ boundary between asteroids and comets is strictly valid only under the assumptions of the circular restricted three-body approximation (in which the only gravitational perturbers are Jupiter and the Sun, and Jupiter's orbit is exactly circular). A more nuanced understanding of T_J and small body dynamics in general, however, is necessary for properly interpreting the implications of small body studies that rely on assumptions about the origin of the small bodies being studied based on this parameter.

The real solar system contains other massive bodies of course, and non-gravitational perturbations from asymmetric outgassing from active bodies or radiative effects can also alter an object's motion in ways that are not accounted for in the circular restricted three-body approximation. As a result, real asteroids and comets are not separated by a sharp dynamical boundary at $T_J = 3$, but instead by a less distinct boundary zone spanning a range of values from $T_J \sim 3.05$ to $T_J \sim 3.10$, with numerical integrations showing that dynamical lifetime distributions of comets with $3.00 < T_J < 3.05$ and comets with $T_J < 3$ are effectively indistinguishable, while comets with $3.05 < T_J < 3.10$ have a mix of short dynamical lifetimes ($t < 2$ Myr), characteristic of objects with $T_J < 3$, and longer dynamical lifetimes ($t > 200$ Myr) characteristic of objects with $T_J > 3.10$ (Figure 10; *Hsieh and Haghighipour* 2016). These results are consistent with the comet-asteroid thresholds of $T_J = 3.05$ and $T_J = 3.08$ used by *Tancredi* (2014) and *Jewitt et al.* (2015), respectively.

Dynamical classification systems based on objects' current orbital parameters can of course be made more complex to try to better capture the dynamical nuances of "true" asteroids and comets (e.g., *Tancredi* 2014), but even these can fail since the idea that an impenetrable boundary in T_J space exists at all between asteroids and comets is fundamentally flawed. Numerical integrations have shown that small bodies can evolve from one side of the T_J boundary to the other, effectively changing their dynamical identities as asteroids or comets as determined by T_J. In a dynamical study of 58 JFCs on near-Earth orbits, *Fernández and Sosa* (2015) found several comets that avoided very close encounters with Jupiter and remained dynamically stable on much longer timescales than other JFCs in the study, and hypothesized that they could have originated in the main asteroid belt. Most of these objects also exhibit rela-
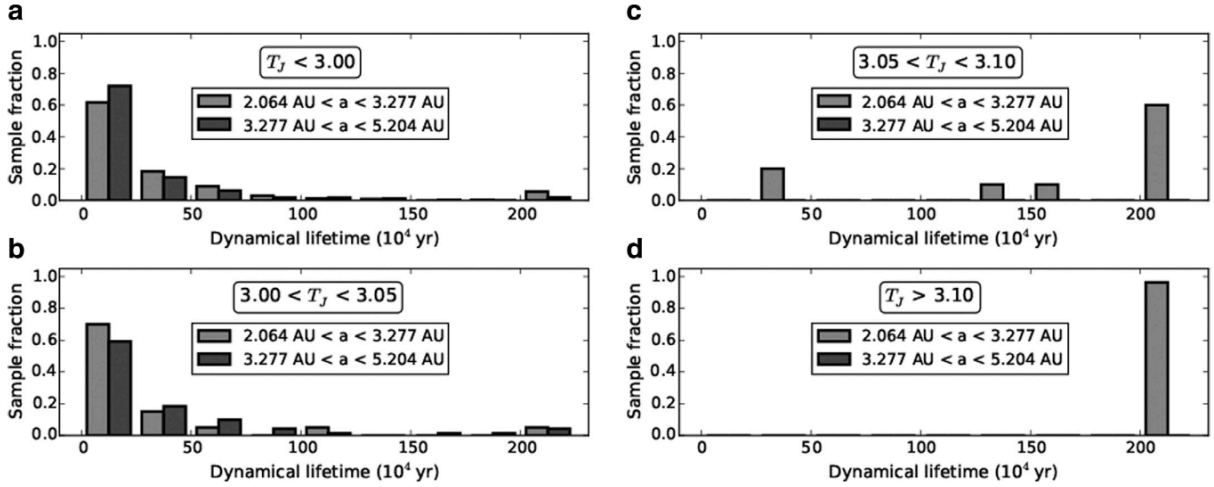
Fig. 10.— Histograms of dynamical lifetimes for known comets with $a \le 5.204$ au with $T_{J,s}$ values of (a) $T_{J,s} < 3.00$, (b) $3.00 < T_{J,s} < 3.05$, (c) $3.05 < T_{J,s} < 3.10$ and (d) $T_{J,s} > 3.10$, where light and dark gray bars indicate the fraction of comets with 2.064 au $< a < 3.277$ au and $a > 3.277$ au, respectively, that are lost due to ejection or planetary/solar impact within a particular time interval. From *Hsieh and Haghighipour* (2016).

tively weak activity for their sizes compared to other JFCs, and some show other asteroid-like physical properties (e.g., 249P/LINEAR; *Fernández et al.* 2017), further supporting possible main-belt origins for those objects.

Numerical integrations performed by *Hsieh et al.* (2020) subsequently revealed a pathway by which transitions inferred by *Fernández and Sosa* (2015) could occur on timescales of <100 Myr. In that pathway (see Figure 11), the 2:1 mean-motion resonance (MMR) with Jupiter can excite the eccentricities of main-belt asteroids (in that work, members of the Themis asteroid family) close to the resonance, lowering their perihelion distances and increasing their aphelion distances. These orbital changes increase the potential for significant interactions with planets other than Jupiter, invalidating the approximation from which the theoretical $T_J = 3$ asteroid-comet boundary is derived, ultimately allowing a small but non-negligible number of objects to evolve from high-T_J orbits to low-T_J orbits.

Statistical evidence (Section 7) indicates that main-belt contamination dominates the population of bodies with $2.8 \le T_J \le 3.0$. A spectroscopic survey by *Licandro et al.* (2008) found that 7 of 41 observed objects with $T_J < 3$ showed absorption bands suggestive of S-type asteroids (known for their distinctly un-comet-like silicate-containing compositions; see *DeMeo et al.* 2015, for a detailed discussion about asteroid taxonomic classification). All seven had $T_J > 2.8$. *Geem et al.* (2021) proposed that asteroids and comets might be distinguished by their polarization vs. phase angle relations, and gave three examples. One of these, (331471) 1984 QY_1, had a small polarization amplitude deemed more characteristic of an S-type asteroid than of a comet. Future measurements might be able to

establish a polarization versus T_J relation that would help distinguish displaced main-belt asteroids from JFCs.

Meanwhile, dynamical evolution of small bodies in the opposite direction, from cometary orbits to asteroidal orbits, also appears to be possible. *Hsieh and Haghighipour* (2016) found that a small number of synthetic test particles with JFC-like initial orbital elements reached fully main-belt-like orbits in 2-Myr-long integrations, suggesting that JFCs could occasionally become interlopers in the main asteroid belt. Such an origin has been suggested for P/2021 A5 (PANSTARRS) (*Moreno et al.* 2021). That said, the JFC interlopers found by *Hsieh and Haghighipour* (2016) are dynamically distinct from the active asteroids in having higher mean eccentricities and inclinations. Efforts to use active asteroids to study primordial volatile material in the asteroid belt (see Section 6.2) might be able to mitigate the impact of such interlopers by focusing only on the low-inclination, low-eccentricity portion of the main belt population.

Even if interactions with all other gravitating solar system bodies are taken into account, non-gravitational accelerations from asymmetric outgassing can cause further deviations from gravity-only dynamical evolution. For example, 2P/Encke is a highly active comet with $T_J = 3.025$, whose unusual orbit *Fernández et al.* (2002) found could be produced from a typical JFC orbit by non-gravitational accelerations, but only if they were sustained for 10^5 years. This physically implausible conclusion (2P does not contain enough ice to remain active that long) was also reached by *Levison et al.* (2006). An astrometric study of 18 active asteroids demonstrated that only two (313P and 324P) exhibited strong evidence of non-gravitational acceleration

(*Hui and Jewitt* 2017). Nevertheless, the possibility that stronger asymmetric mass loss in the past could have produced their current asteroid-like orbits cannot be ruled out.

In summary, as with other binary criteria for distinguishing comets and asteroids (see Sections 2, 3, and 4), dynamical classification is also not always clear-cut. Orbit evolution is an intrinsically chaotic, and therefore non-deterministic, process. Backward and forward numerical integrations can indicate what range of past and future dynamical evolution is possible (with dynamical clones typically used for this purpose), but cannot track an object's exact dynamical origin or fate beyond a certain length of time. Conclusions about a specific object's origin are unavoidably statistical in nature.
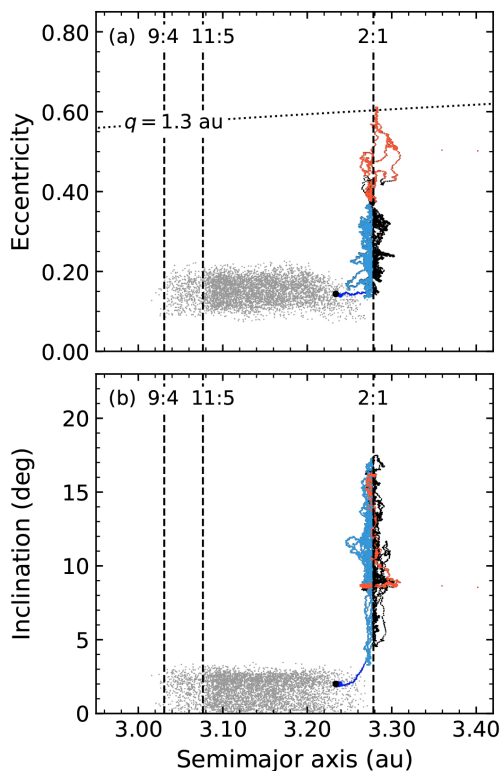

Fig. 11.— Plots of the forward dynamical evolution of Themis family asteroid (12360) Unilandes in (a) semimajor axis vs. eccentricity space, and (b) semimajor axis vs. inclination space. Large black circles in each panel mark the current orbital elements of the asteroid, gray dots mark the current orbital elements of Themis family asteroids, and other colored dots mark intermediate orbital elements in the forward integrations of the object. Of the latter, blue dots mark intermediate orbital elements meeting criteria for being classified main-belt-like, and red dots mark orbital elements that meet criteria (including $T_J < 3$) for being classified as JFC-like. From *Hsieh et al.* (2020).

6. ACTIVE ASTEROIDS

6.1. Overview

Active asteroids have dynamical properties characteristic of asteroids and the physical appearances of comets. They are one of the more recent groups of objects to be recognized as blurring the lines between asteroids and comets, although many individual objects in this category were known long before the term "active asteroid" was first used. A wide range of potential mechanisms for the observed comet-like mass loss of active asteroids has been identified, including sublimation (Section 3.2), impacts (Section 3.3), rotational instability (Section 3.4), thermal fracture (Section 3.7), and combinations of these processes, making these objects valuable for the opportunities they provide to study these processes in the real world. Reviews addressing different aspects of activity in asteroids include *Jewitt* (2004), *Jewitt* (2012), *Jewitt et al.* (2015), and *Kasuga and Jewitt* (2019). Table 1 lists the active asteroids known as of 2022 January 1, while their distribution in semi-major axis versus eccentricity space is shown in Figure 12.

6.2. Main-Belt Comets

The main-belt comets (MBCs) are a noteworthy subset of the active asteroids, comprising objects for which sublimation appears to plays a role in producing the observed mass loss (*Hsieh and Jewitt* 2006). The nature of their activity and largely stable orbits in the main asteroid belt indicate that near-surface volatile material has managed to remain preserved in the inner solar system until the present day. They have attracted significant scientific interest since their discovery due to the opportunities they provide to place constraints on the volatile content of inner solar system bodies and their possible connections to the primordial delivery of water and other volatile material to the early Earth (e.g., *Hsieh* 2014a).

The MBCs discovered to date are too weakly active (production rates $\lesssim 1$ kg s^{-1} compared with 10^2 to 10^3 kg s^{-1} for typical comets) for gas to be spectroscopically detected given the sensitivity limits of current ground-based telescopes (*Jewitt* 2012). Instead, the most distinctive observational property of the MBCs is repeated near-perihelion activity in different orbits, indicating that their activity is thermally modulated (see Section 3.2). Of the many processes considered in Section 3, only temperature-dependent sublimation can easily account for repeated near-perihelion activity. Independent evidence for outgassing comes from the detection of non-gravitational acceleration (caused by recoil from the anisotropic mass loss) in 313P/Gibbs and 324P/La Sagra (*Hui and Jewitt* 2017). Only gas carries enough momentum to explain the observed non-gravitational accelerations. Evidence for sublimation as the driver of activity in MBCs is thus indirect but compelling. Reviews specifically focusing on MBCs include *Bertini* (2011) and *Snodgrass et al.* (2017). MBCs iden-
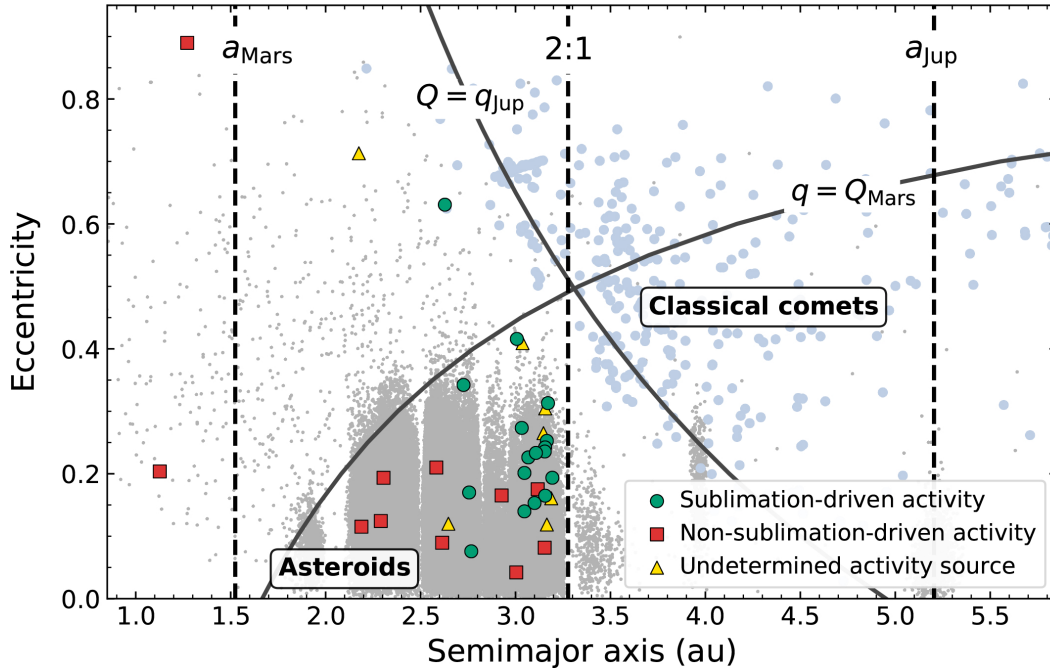
Fig. 12.— Semimajor axis vs. orbital eccentricity plot for active asteroids determined to exhibit likely sublimation-driven activity (open green circles), activity driven by processes other than sublimation (open red squares), and activity of currently undetermined origin (open yellow triangles), where classical comets are marked as filled light blue circles and asteroids as small gray dots. Curved arcs show the loci of points having aphelion and perihelion distances equal to the aphelion of Mars and the perihelion of Jupiter, respectively, as marked. Objects above these lines cross the orbits of those planets. Vertical dashed lines mark the orbital radii of Mars and Jupiter and the location of the 2:1 mean-motion resonance with Jupiter.

tified through the repetition of their activity in more than one orbit or through other means (e.g., dust modeling indicating prolonged dust emission events characteristic of sublimation-driven activity) are shown as green symbols in Figure 12.

The "duty cycle", f_{dc}, defined as the fraction of the total time during which an MBC is active, is an important quantity because it is related to the abundance of ice in the asteroid belt. Values of $f_{dc} \ll 1$ are automatically required in order for the MBCs to have survived against devolatilization (*Hsieh and Jewitt* 2006) or destruction by spin-up (*Jewitt et al.* 2019c). The most stringent estimates, $f_{dc} \lesssim 3 \times 10^{-5}$, are obtained from surveys conducted in search of asteroid activity (*Gilbert and Wiegert* 2010; *Waszczak et al.* 2013). Such small values identify the MBCs as the tip of the proverbial iceberg; each detected MBC represents $f_d^{-1} \gtrsim 30,000$ similarly icy asteroids that were not detected as such because they exist in the dormant state. It is entirely possible, for example, that *all* outer-belt asteroids contain ice and that the MBCs are notable simply because we observe them in an unusual outgassing state. Additional characteristics (e.g., fast rotation, small nucleus sizes and therefore low escape velocities, moderate orbital eccentricities, small obliquities, membership in young asteroid families, and so on; *Hsieh et al.* 2004, 2018c; *Hsieh*

2009; *Kim et al.* 2018; *Schörghofer* 2016), may aggregate to help produce observable activity.

6.3. Active Asteroid Examples

6.3.1. Sublimation: 133P/(7968) Elst-Pizarro

Comet 133P/(7968) Elst-Pizarro, originally discovered as asteroid 1979 OW_7, was first found to exhibit comet-like activity on 1996 August 7, shortly after passing perihelion on 1996 April 18 (*Elst et al.* 1996). At the time, 133P was the first and only main-belt asteroid observed to exhibit comet-like activity, leading to uncertainty about whether the observed mass loss, later determined to have occurred over the course of several weeks or months (*Boehnhardt et al.* 1996), was due to sublimation of volatile material similar to other comets, or to a series of impacts (*Toth* 2000). Follow-up observations in 2002 revealed 133P to be active (*Hsieh et al.* 2004), again near perihelion, heavily favoring the hypothesis that its activity was due to the sublimation of exposed volatile material, instead of a highly improbable succession of impacts. Since then, 133P has continued to exhibit activity at each of its subsequent perihelion passages (e.g., *Hsieh et al.* 2010; *Jewitt et al.* 2014b), firmly establishing the recurrent and likely sublimation-driven nature of its activity.

Table 1: Currently Known Active Asteroids

Object	a[a]	e[b]	i[c]	T_J[d]	H_V[e]	r_n[f]	$P_{\rm rot}$[g]	Mech.[h]	Ref.[i]
(1) Ceres	2.766	0.078	10.588	3.310	3.53	469.7	9.07	S	[1]
(493) Griseldis	3.116	0.176	15.179	3.140	10.97	20.78	51.94	I	[2]
(596) Scheila	2.929	0.163	14.657	3.209	8.93	79.86	15.85	I	[3]
(2201) Oljato	2.174	0.713	2.522	3.299	15.25	0.90	>26.	—	[4]
(3200) Phaethon	1.271	0.890	22.257	4.510	14.32	3.13	3.60	RTP	[5]
(6478) Gault	2.305	0.193	22.812	3.461	14.81	2.8	2.49	R(I)	[6]
(62412) 2000 SY$_{178}$	3.159	0.079	4.738	3.195	13.74	5.19	3.33	R(SI)	[7]
(101955) Bennu	1.126	0.204	6.035	5.525	20.21	0.24	4.29	(ITP)	[8]
107P/(4015) Wilson-Harrington	2.625	0.632	2.799	3.082	16.02	3.46	7.15	S	[9]
133P/(7968) Elst-Pizarro	3.165	0.157	1.389	3.184	15.49	1.9	3.47	SR(E)	[10]
176P/(118401) LINEAR	3.194	0.193	0.235	3.167	15.10	2.0	22.23	S(IE)	[11]
233P/La Sagra (P/2005 JR$_{71}$)	3.033	0.411	11.279	3.081	~16.6	~1.5	—	—	[12]
238P/Read (P/2005 U1)	3.162	0.253	1.266	3.153	19.05	0.4	—	S(IR)	[13]
259P/Garradd (P/2008 R1)	2.727	0.342	15.899	3.217	19.71	0.30	—	S(IR)	[14]
288P/(300163) 2006 VW$_{139}$	3.051	0.201	3.239	3.203	~17.8,~18.2	~0.9,~0.6	—	S	[15]
311P/PANSTARRS (P/2013 P5)	2.189	0.116	4.968	3.660	19.14	0.2	>5.4	R	[16]
313P/Gibbs (P/2014 S4)	3.154	0.242	10.967	3.133	17.1	1.0	—	S(R)	[17]
324P/La Sagra (P/2010 R2)	3.098	0.154	21.400	3.099	18.4	0.55	—	S(R)	[18]
331P/Gibbs (P/2012 F5)	3.005	0.042	9.739	3.228	17.33	1.77	3.24	R	[19]
354P/LINEAR (P/2010 A2)	2.290	0.125	5.256	3.583	—	0.06	11.36	I	[20]
358P/PANSTARRS (P/2012 T1)	3.155	0.236	11.058	3.134	19.5	0.32	—	S(R)	[21]
426P/PANSTARRS (P/2019 A7)	3.188	0.161	17.773	3.103	~17.1	~1.2	—	—	[22]
427P/ATLAS (P/2017 S5)	3.171	0.313	11.849	3.092	18.91	0.45	1.4	SR	[23]
432P/PANSTARRS (P/2021 N4)	3.045	0.244	10.067	3.170	>18.2	<0.7	—	—	[24]
433P/(248370) 2005 QN$_{173}$	3.067	0.226	0.067	3.192	16.32	1.6	—	S(RI)	[25]
P/2013 R3 (Catalina-PANSTARRS)	3.033	0.273	0.899	3.184	—	~0.2 (×4)	—	SR	[26]
P/2015 X6 (PANSTARRS)	2.755	0.170	4.558	3.318	>18.2	<0.7	—	S(IR)	[27]
P/2016 G1 (PANSTARRS)	2.583	0.210	10.968	3.367	—	<0.4	—	I	[28]
P/2016 J1-A/B (PANSTARRS)	3.172	0.228	14.330	3.113	—	<0.4,<0.9	—	S(IR)	[29]
P/2017 S9 (PANSTARRS)	3.156	0.305	14.138	3.087	>17.8	<0.8	—	—	[30]
P/2018 P3 (PANSTARRS)	3.007	0.416	8.909	3.096	>18.6	<0.6	—	S(IR)	[31]
P/2019 A3 (PANSTARRS)	3.147	0.265	15.367	3.099	>19.3	<0.4	—	—	[32]
P/2019 A4 (PANSTARRS)	2.614	0.090	13.319	3.365	—	0.17	—	(IR)	[33]
P/2020 O1 (Lemmon-PANSTARRS)	2.647	0.120	5.223	3.376	>17.7	<0.9	—	—	[34]
P/2021 A5 (PANSTARRS)	3.047	0.140	18.188	3.147	—	0.15	—	S(IR)	[35]
P/2021 L4 (PANSTARRS)	3.165	0.119	16.963	3.125	>15.8	<2.2	—	—	[36]
P/2021 R8 (Sheppard)	3.019	0.294	2.203	3.179	—	—	—	—	[37]

[a] Semimajor axis, in au.   [b] Eccentricity.   [c] Inclination, in degrees.   [d] Tisserand parameter with respect to Jupiter.

[e] Measured V-band absolute magnitude, or estimated upper limit based on apparent brightness when active, if available.

[f] Effective nucleus radius (or radii), in km, as estimated from absolute magnitude or via other means as described in references.

[g] Rotation period, in hr, if available.

[h] Mechanisms likely contributing to the observed activity (S: sublimation; I: impact; R: rotational destabilization; E: electrostatics; T: thermal fatigue/fracturing; P: phyllosilicate dehydration); mechanisms enclosed in parentheses are not directly indicated, but are not excluded by available data

[i] References: [1] *Küppers et al.* (2014); *Park et al.* (2016); [2] *Tholen et al.* (2015); [3] *Ishiguro et al.* (2011a);
[4] *Russell et al.* (1984); *Tedesco et al.* (2004); *Warner et al.* (2019); [5] *Jewitt and Li* (2010); *Ansdell et al.* (2014);
[6] *Devogèle et al.* (2021); [7] *Sheppard and Trujillo* (2015); [8] *Lauretta et al.* (2019); [9] *Fernández et al.* (1997);
Licandro et al. (2009); *Urakawa et al.* (2011); [10] *Hsieh et al.* (2004, 2009a, 2010); [11] *Hsieh et al.* (2009a, 2011a);
[12] *Mainzer et al.* (2010); [13] *Hsieh et al.* (2011b); [14] *MacLennan and Hsieh* (2012); *Hsieh et al.* (2021b);
[15] *Agarwal et al.* (2020); [16] *Jewitt et al.* (2018b); [17] *Hsieh et al.* (2015b); [18] *Hsieh* (2014b);
[19] *Drahus et al.* (2015); [20] *Jewitt et al.* (2010b); *Snodgrass et al.* (2010); *Kim et al.* (2017a,b);
[21] *Hsieh et al.* (2013, 2018b); [22] *Rudenko et al.* (2021); [23] *Jewitt et al.* (2019c); [24] *Wainscoat et al.* (2021);
[25] *Hsieh et al.* (2021a); [26] *Jewitt et al.* (2014a); [27] *Moreno et al.* (2016a); [28] *Moreno et al.* (2016b);
Hainaut et al. (2019); [29] *Moreno et al.* (2017); *Hui et al.* (2017); [30] *Weryk et al.* (2017); [31] *Weryk et al.* (2018);
Kim et al. (2019); [32] *Weryk et al.* (2019); [33] *Moreno et al.* (2021); [34] *Weryk et al.* (2020); [35] *Moreno et al.* (2021);
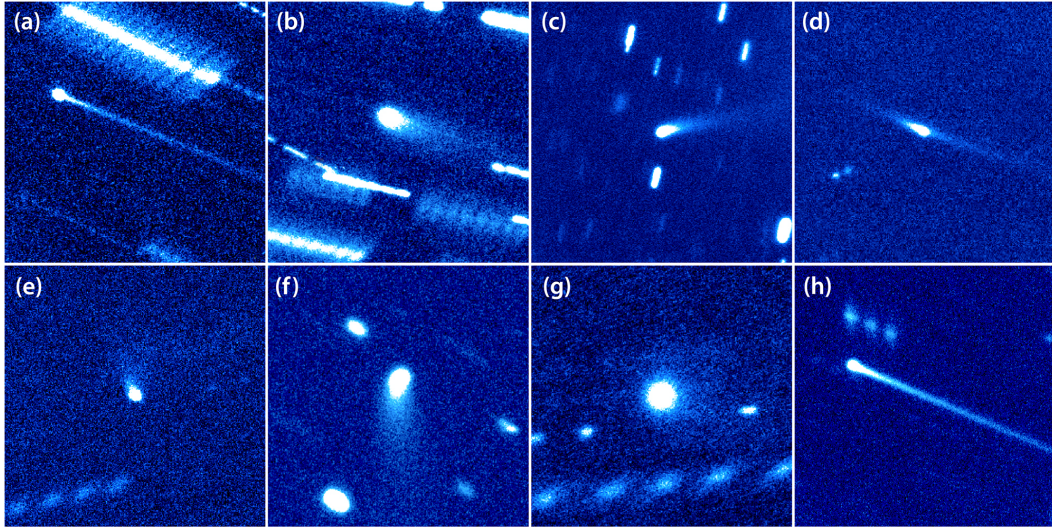[36] *Wainscoat et al.* (2021) [37] *Tholen et al.* (2021)

Fig. 13.— Gallery of $1' \times 1'$ images of MBCs confirmed to exhibit recurrent activity: (a) 133P/Elst-Pizarro, (b) 238P/Read, (c) 259P/Garradd, (d) 288P/(300163) 2006 VW$_{139}$, (e) 313P/Gibbs, (f) 324P/La Sagra, (g) 358P/PANSTARRS, and (h) 433P/(248370) 2005 QN$_{173}$. Images adapted from data published in *Hsieh et al.* (2004, 2009b, 2012b,c, 2013, 2015b, 2021a,b).

Calculations described in Section 3.2 show that sublimation rate differences between perihelion and aphelion for main belt asteroids can easily explain the preferential appearance of detectable activity only near perihelion, while obliquity-related and surface-shadowing effects may also play a role. To date, seven other active asteroids (Figure 13) have been found to exhibit recurrent activity near perihelion (Figure 3; see *Hsieh et al.* 2021a), indicating that they are likely MBCs exhibiting sublimation-driven mass loss, and corroborating the hypothesis that their activity is primarily modulated by temperature and not seasonal effects.

Interestingly, 133P's relatively fast rotation rate of $P_{\rm rot} = 3.471$ hr (*Hsieh et al.* 2004) suggests that rotational instability could assist in the ejection of dust particles initially lofted by sublimation. Combined with the hypothesis that 133P's current activity may have required an initial collisional trigger to excavate a sub-surface ice reservoir (see Section 3.2), 133P presents an excellent illustrative case of an active object for which multiple mechanisms may be responsible for observed activity.

6.3.2. Impact: 354P/LINEAR and (596) Scheila

Comet 354P/LINEAR (formerly P/2010 A2) and (596) Scheila were the first objects discovered immediately following impact events. The largest component in 354P's debris cloud is $\sim$100 m in scale, and is accompanied by a co-moving cluster of smaller bodies embedded in a particle trail (*Jewitt et al.* 2010b; *Snodgrass et al.* 2010; *Jewitt et al.* 2013b). The object was disrupted by a collision nine months before it was discovered, with the delay in the dis-
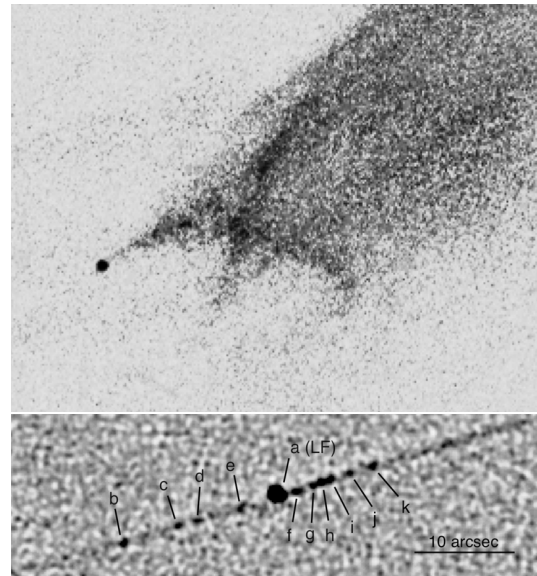

Fig. 14.— (top) Head structure of P/2010 A2 on UT 2010 January 25, from *Jewitt et al.* (2010b). (bottom) fragments in the particle trail on UT 2017 January 27 and 28, from *Kim et al.* (2017a).

covery in part due to having an initially small solar elongation (*Jewitt et al.* 2011a). While rotational destabilization was also initially considered as a possible alternate explanation for 354P's activity (*Jewitt et al.* 2010b), the main nucleus was later found to have a double-peaked rotational period of $P_{\rm rot} = 11.36 \pm 0.02$ hr, ruling out fast rotation as a potential cause of the observed activity (*Kim et al.* 2017a).

18

Meanwhile, the 113 km diameter asteroid 596 Scheila ejected $\sim 10^8$ kg of dust due to an apparent cratering impact in late 2010 (*Jewitt et al.* 2011b), with that dust clearing in a few weeks. The impulsive nature of the brightening and the monotonic fading thereafter are consistent with the impact of a 20 m t0 40 m-scale projectile. The unusual dust cloud morphology exhibited by Scheila can be reproduced by an impact ejecta cone and downrange plume produced by an impact at a $\sim 45°$ angle to the object's surface (*Ishiguro et al.* 2011a). *Ishiguro et al.* (2011b) and *Bodewits et al.* (2014) also reported post-impact changes in the optical lightcurve while *Hasegawa et al.* (2021b) reported a reddening in the 1.0 to 2.5 μm wavelength region, but, curiously, no change from 0.4 to 1.0 μm or from 2.5 to 4.0 μm. If real, the observed lightcurve modifications may have resulted from fallback of material ejected at speeds less than Scheila's $\sim$60 m s^{-1} escape velocity, while the reported near-infrared color change, might suggest burial of a surface previously de-reddened by space weathering.

The discoveries of these two objects, both in 2010, represent a key milestone in our understanding of the comet-asteroid continuum, as they definitively demonstrated for the first time that impact events could be detected in real time, and also that observations of comet-like activity do not always mean that sublimation of volatile material is taking place. This realization helped to pave the way for other non-sublimation-related interpretations of future activity detections (Sections 3, 6.3.3, and 6.3.4).

6.3.3. *Rotational Breakup: P/2013 R3 (Catalina-PANSTARRS)*

Perhaps the most dramatic example of rotational destabilization found to date is P/2013 R3 (Catalina-PANSTARRS), which was observed in 2013 in the midst of disintegrating into a collection of $\sim 10^2$ m scale bodies with a velocity dispersion of $\Delta V \sim 0.3$ m s^{-1} (Figure 15; *Jewitt et al.* 2014a). The parent body size is estimated at a few $\times 10^2$ m. Bodies this small are susceptible to spin-up by radiation torques on timescales $\lesssim 1$ Myr, leading to the suspicion that P/2013 R3 was a rotationally disrupted asteroid. Sublimating water ice, if present, could also spin up the body on a very short timescale (*Jewitt* 2021), and in fact was inferred to be present by the dust ejection behavior of individual components of the object as it disintegrated (*Jewitt et al.* 2014a). Modeling of the break-up process by *Hirabayashi et al.* (2014) suggested that the parent body had a rotational period of $0.48-1.9$ hr, implying that it was likely spinning well beyond the critical disruption limit for a rubble pile prior to its breakup, suggesting that the object had some degree of cohesive strength on the order of $40-210$ Pa, comparable to the cohesion expected of a sand pile. Similar to 133P (Section 6.3.1), P/2013 R3 presents an interesting case where multiple activity mechanisms are operating,

with rotational instability likely being the primary cause of the disintegration of the parent body, but with continued decay and dust release then driven by sublimation of interior ices exposed by the disruption event.
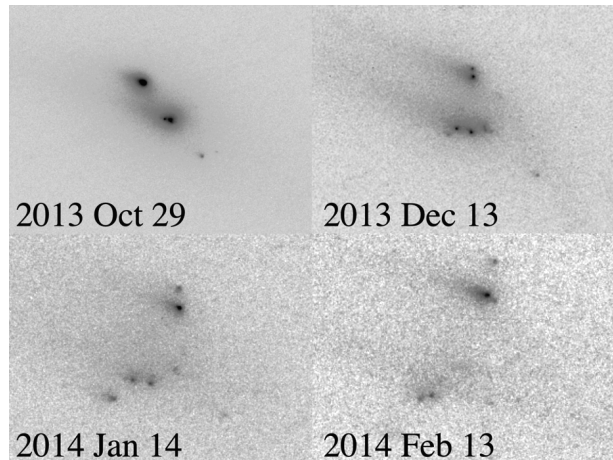

Fig. 15.— Fragments of P/2013 R3 on four dates, as marked. Each panel shows a region approximately 20,000 km wide. The anti-solar and negative projected orbit vectors are at position angles 67° and 246°, respectively. North to the top, East to the left. From *Jewitt et al.* (2017).

6.3.4. *Rotational Instability: (6478) Gault, 331P/Gibbs and 311P/PANSTARRS*

Non-catastrophic mass loss events observed for main-belt asteroid (6478) Gault and comets 311P/PANSTARRS and 331P/Gibbs were all believed to be produced by rotational destabilization, yet were simultaneously remarkably diverse compared to one another (as well as compared to the catastrophic rotational disruption of P/2013 R3; Section 6.3.3). The diversity in active behavior displayed by these three objects demonstrates the complexity of rotational destabilization as an activity mechanism, with potentially very different outcomes depending on the circumstances of each object and event.

Comet 311P (formerly P/2013 P5) displayed a distinctive set of discrete dust tails (Figure 16), formed by submillimeter-sized debris ejected in nine bursts over nine months, with no evidence of periodicity in the mass-loss events and no evidence for macroscopic fragments in the ejecta (*Jewitt et al.* 2013a). The directions of the tails are determined by the ejection epoch and the subsequent action of radiation pressure, creating a size gradient along each tail. 311P's activity likely resulted from the loss of loose surface material which avalanched to the equator in response to rapid rotation. A reliable period has not been determined for 311P. Instead, photometry of its nucleus shows complex structure, suggestive of an eclipsing, possibly contact, binary (*Jewitt et al.* 2018b).
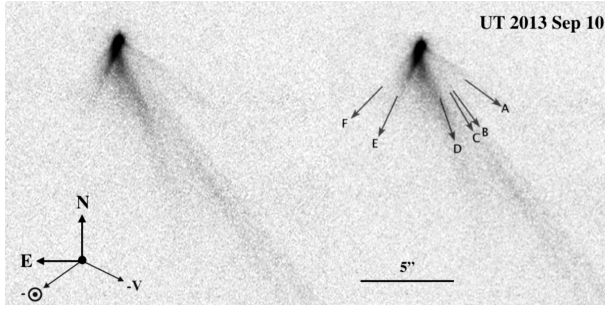
Fig. 16.— Multi-tailed active asteroid 311P. The first six of nine tails are labeled. From *Jewitt et al.* (2013a).
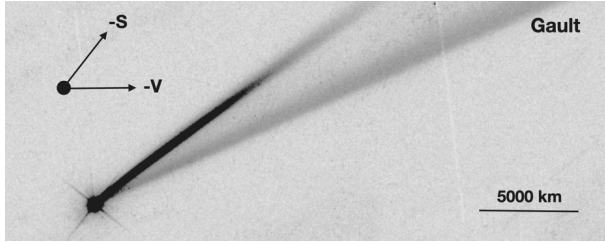

Fig. 17.— Gault on UT 2019 February 5, showing two of the three tails ejected in 2019. From *Kleyna et al.* (2019).

Meanwhile, when discovered to be active in 2019, Gault exhibited two bright tails (Figure 17; e.g., *Kleyna et al.* 2019), while a third, fainter tail emerged in later follow-up imaging (*Jewitt et al.* 2019b). Intriguingly, searches of archival data revealed multiple additional past mass loss events over six years (*Chandler et al.* 2019). Like for 311P, the episodic nature of Gault's dust ejection events, as well as a lack of evidence that other activity mechanisms such as sublimation could be driving the observed activity, indicated that its activity was likely to be driven by rotational destabilization. This hypothesis was later supported by observations of the nucleus after activity had subsided, revealing an extremely short rotational period of $P_{rot} = 2.5$ hr with a lightcurve amplitude of 0.06 mag (*Devogèle et al.* 2021; *Luu et al.* 2021). Together, these observations suggest that Gault is a rapidly spinning asteroid held continuously at the brink of rotational disruption, perhaps by the YORP effect, that periodically undergoes mass loss events that temporarily restabilize it. Unlike the eight MBCs showing confirmed recurrent activity near perihelion (Section 6.2), activity in Gault is unrelated to its heliocentric distance, evidently because sublimation does not play a role in its activity.

331P/Gibbs ejected only a small fraction of the parent body mass ($\Delta M/M \sim 0.01$), visible as a set of fragments embedded in a long debris trail (Figure 18; *Jewitt et al.* 2021). The 0.8 km radius (assuming an albedo of 0.05)

primary body again shows clear evidence of rapid rotation, with period $P_{rot} = 3.26$ hr. At this period, Equation 8 gives $\rho = 1600$ kg m^{-3} as the minimum density required for a cohesionless spherical body to resist mass shedding at its equator. The 19 measurable fragments ejected from 331P travel away from the source at incredibly low speeds, ~ 0.1 m s^{-1}. The fragments show no sign of further fading or disintegration over a three year window of observation, consistent with having wholly refractory compositions. The largest, the 100 m scale 331P-A (visible as the second brightest object in Figure 18), shows a large-amplitude rotational lightcurve with morphological characteristics consistent with a contact binary structure. They are embedded in a debris trail, also characterized by a small velocity dispersion. Despite its designation, "comet" 331P is probably a non-volatile, rotationally unstable asteroid.

6.3.5. Thermal Breakdown: (3200) Phaethon

The Geminid meteoroid stream consists of millimeter-sized and larger debris with a total mass $M_G \sim$ (2 to 7)$\times 10^{13}$ kg (*Blaauw* 2017). The stream is $\tau \sim 10^3$ years old, as judged by the spread of orbital elements of the Geminid meteors (*Gustafson* 1989; *Williams and Wu* 1993) and, to be supplied in steady state, would require production at the rate $M_G/\tau \sim$700 to 2000 kg s^{-1}. Such large rates would be comparable to those of bright comets, but no such bright comet source of the Geminids exists. Instead, the Geminids appear to be supplied by the 5 to 6 km diameter B-type asteroid (3200) Phaethon.

Curiously, dark sky observations have consistently shown no visible evidence for on-going mass loss from Phaethon at the $\sim 10^{-2}$ kg s^{-1} level (*Hsieh and Jewitt* 2005), or even from the vantage point of a near-Earth (0.07 au) flyby in 2017, where limits $\leq 10^{-3}$ kg s^{-1} were set (*Jewitt et al.* 2018a, 2019a). However, observations near perihelion at $r_H = 0.14$ au (Figure 9) show photometric behavior and a resolved tail consistent with the release of μm-sized particles at about 3 kg s^{-1} (*Jewitt and Li* 2010; *Li and Jewitt* 2013; *Jewitt et al.* 2013b; *Hui and Li* 2017). This rate is still two to three orders of magnitude too small to supply the Geminids in steady state. Furthermore, the μm-sized particles detected near perihelion are so strongly affected by solar radiation pressure that they cannot be confined to the Geminid stream. Either the particle size distribution is shallow, such that unseen large particles dominate the ejected mass or, more likely, the source of the Geminids is episodic, or even catastrophic in nature, and unrelated to the activity at perihelion.

Several mechanisms have been suggested to drive Phaethon's observed repeated perihelion activity. The subsolar temperature on Phaethon is ~ 1000 K, suggesting that stresses induced by thermal expansion and desiccation shrinkage could eject fragments (*Jewitt and Li* 2010; *Jewitt*
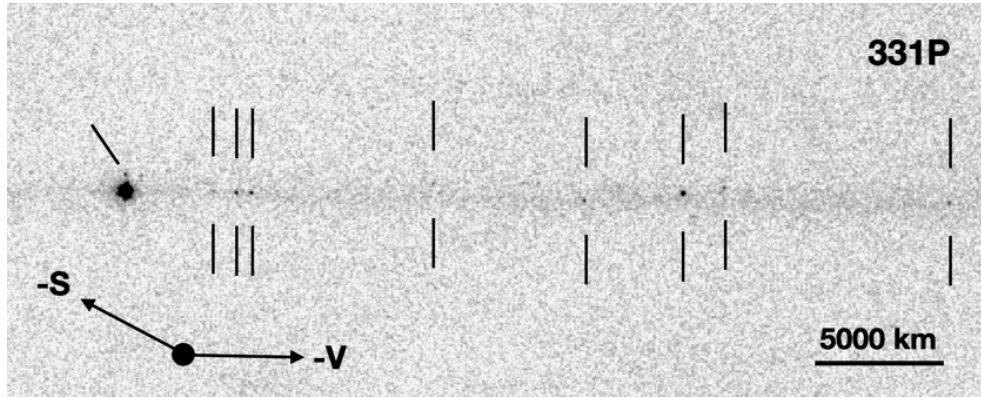
Fig. 18.— Some of the 19 fragments of 331P on UT 2013 December 25. The fragments, many of which are very faint and only confirmed by their reappearance in images from different dates, are marked by solid black lines. The 1.6±0.2 km diameter primary is the bright object to the left. Suspected contact binary 331P-A is third from the right. From *Jewitt et al.* (2021).

2012). Sublimation of mineralogically bound sodium could also eject small dust particles through gas drag (*Masiero et al.* 2021), provided that there is enough mineralogically bound sodium and that a mechanism exists to replenish quickly-depleted surface materials with sodium-rich minerals. Phaethon's $P_{\rm rot} = 3.6$ hr rotation period (*Ansdell et al.* 2014) suggests that centrifugal effects might also contribute to mass loss (*Nakano and Hirabayashi* 2020), as does its likely top-shape (*Hanuš et al.* 2016; *Taylor et al.* 2019).

Phaethon's dynamical lifetime is $\lesssim 10^8$ years, implying delivery from elsewhere in the solar system (*de León et al.* 2010). A cometary origin is unlikely, given that the orbit is strongly decoupled from Jupiter, and has the very large Tisserand parameter $T_J = 4.5$. However, the specific source region, presumably in the main asteroid belt, is unknown. Suggested sources include the large B-type asteroid 2 Pallas (*de León et al.* 2010) and, more likely, a collisional family in the inner asteroid belt (*MacLennan et al.* 2021). The km-sized asteroid 2005 UD appears dynamically related to Phaethon (*Ohtsuka et al.* 2006) and is coincidentally also a B-type object (*Jewitt and Hsieh* 2006), (although recent observations show dissimilarity in the near infrared; *Kareta et al.* 2021). A dynamical relation to another kilometer-sized asteroid, 1999 YC, has also been proposed but is less certain, where 1999 YC is a neutral C-type spectrally distinct from the blue B-types Phaethon and 2005 UD (*Kasuga and Jewitt* 2008).

Phaethon, 2005 UD and the Geminid stream are collectively known as the "Phaethon-Geminid Complex" (*Ohtsuka et al.* 2006). Unfortunately, the genetic relationships between these bodies remain completely unknown, as does the relevance of the current mass loss from Phaethon at perihelion (*Kasuga and Jewitt* 2019). We hope for clarification of the nature of Phaethon's surface by the upcoming DESTINY+ flyby mission (see Section 9), although the 33

km s^{-1} encounter velocity and planned 500 km distance of closest approach will limit the data obtained.

6.3.6. Unknown: (101955) Bennu

Repeated instances of particle ejection from Bennu were observed from the OSIRIS-REx spacecraft (Figure 2; *Lauretta et al.* 2019). Particles ejected from Bennu, estimated to be cm-sized, were emitted erratically, with one large burst containing up to 200 particles. Particle speeds were estimated to range from 0.1 m s^{-1} to 3 m s^{-1}, with $\sim$70% of the particles being too slow to escape and falling back to the surface. The peak observed ejection velocity, 3 m s^{-1}, exceeded the 0.2 m s^{-1} escape velocity from Bennu by an order of magnitude. Dissimilar size distributions were measured in three outburst events, with differential power laws indices varying from -3.3 to -1.2 (*Hergenrother et al.* 2020). The total ejected mass, however, was very small. *Hergenrother et al.* (2020) estimated a mass loss of ~ 10 kg per orbit, corresponding to a mean mass loss rate of $\dot{M} \sim 10^{-7}$ kg s^{-1} over the 1.2 year orbit period. This is $\sim 10^6$ to 10^7 times smaller than the sensitivity limits achieved through ground-based observations of other active asteroids.

The chance, in-situ discovery of Bennu's activity raises the possibility that many asteroids lose mass at rates that are individually beneath the ground-based detection threshold. To consider the possible magnitude of low-level dust production across the asteroid belt, we scale the surface area of Bennu ($\sim$1 km^2) to the total surface area of all asteroids having escape velocities less than the peak ejection velocities of Bennu ejecta. The latter corresponds to a radius of $r_n < 3$ km. This total area, calculated by integrating over the asteroid size distribution, is $\sim 10^8$ km^2. Therefore, if all $r_n \leq 3$ km asteroids eject dust at the same rate as Bennu, the total mass loss would be $10^8(\dot{M}) \sim 10$ kg s^{-1}.

While this is a very crude calculation, it serves to show that Bennu-like production of dust in the asteroid belt is, at best, a very minor contributor to the 10^3 to 10^4 kg s^{-1} production rate needed to sustain the Zodiacal cloud (*Nesvorný et al.* 2011). We also note that the Hayabusa2 spacecraft (*Tsuda et al.* 2019) did not detect any Bennu-like loss of particles from (162173) Ryugu during its encounter with the asteroid in 2018-2019, despite the fact that Ryugu is also taxonomically classified as a primitive asteroid (*Watanabe et al.* 2019) and was also observed in situ by a visiting spacecraft. We do not know if this reflects an intrinsic difference between the two asteroids, or merely a difference in the sensitivity to small particles between the two spacecraft.

The mechanism driving Bennu's mass loss is currently undetermined, despite the availability of abundant spacecraft data. The primary constraints are the sizes, numbers and speeds of the ejected fragments, as well as an apparent preference for launch in the local afternoon. Of the mechanisms already proposed for the active asteroids, electrostatic lofting, micrometeorite impact (*Bottke et al.* 2020), thermal fracture and dehydration cracking (*Molaro et al.* 2020) have all been considered in the case of Bennu.

7. INACTIVE COMETS

The average dynamical lifetimes of short-period comets exceed their volatile lifetimes. Therefore, the fate of old comets, if they do not disintegrate completely, is to leave behind inert, asteroid-like bodies travelling in comet-like orbits. These are the ACOs and Damocloids mentioned in Section 1. Proper identification of such objects is essential for setting constraints on the physical lifetimes of comets (e.g., *Jewitt* 2004) and models of cometary source regions (e.g., *Wang and Brasser* 2014; *Brasser and Wang* 2015). ACOs and Damocloids are presumed to be comets for which activity has weakened below detectable limits or completely ceased due to the depletion of surface volatiles or mantling (e.g., *Podolak and Herman* 1985; *Prialnik and Bar-Nun* 1988; *Jewitt* 1996), although other processes like hydrostatic compression have also been proposed to contribute to activity quenching (*Gundlach and Blum* 2016).

Table 2 lists the numbers of asteroids, N_a, and comets, N_c, compiled from the JPL Horizons orbital element database (https://ssd.jpl.nasa.gov/horizons/), together with their ratio, $\mathcal{R} = N_a/N_s$, all as functions of the binned Tisserand parameter, T_J. The listed uncertainty on $\mathcal{R}$ has been calculated assuming Poisson counting statistics. In this table, asteroids and comets are distinguished only by whether or not visible activity has ever been reported. Objects with large perihelia, even those known from detailed observations to be active comets, are too cold and weakly active for outgassing to be easily measured. Therefore, in order to make the empirical asteroid/comet distinction meaningful, we only list objects with perihelia $q \leq 2.0$ au, where

Table 2: Empirical Asteroid:Comet Ratio vs. T_J [1]

T_J	N_a[2]	N_c[3]	$\mathcal{R}$[4]
<1	28	372	0.08±0.01
<2	453	108	0.24±0.02
2.0 - 2.2	55	7	7.9±3.2
2.2 - 2.4	101	23	4.4±1.0
2.4 - 2.6	202	38	5.3±0.9
2.6 - 2.8	553	75	7.4±0.9
2.8 - 3.0	2727	89	30.6±3.3
>3	315331	12	2.6×10^4

[1] Perihelion $q < 2$ au only
[2] Number of asteroids
[3] Number of comets
[4] Ratio $\mathcal{R} = N_a/N_c$

activity is relatively easy to detect. We also exclude from consideration the sungrazing comets, which generally have poorly determined orbits. The table provides a first-order estimate of the asteroid/comet number ratio as a function of a simple dynamical parameter.

As expected, the Table shows that almost all objects with $T_J > 3$ are asteroids ($\mathcal{R} \gg 1$), while most of those with $T_J < 2$ are comets ($\mathcal{R} < 1$). In between, $\mathcal{R}$ is roughly constant across the range assigned to the JFCs (namely $2 \leq T_J \leq 3$) except for a higher value ($\mathcal{R} = 31$) in the range $T_J > 2.8$ to 3.0. This is presumably because of contamination of the $2.8 \leq T_J \leq 3.0$ sample by scattered main-belt asteroids (see Section 5). An independent study of objects with $q < 1.3$ au also finds that $T_J \sim 2.8$ marks a change in the spectral characteristics, with featureless C and X type spectra more common at $T_J < 2.8$ than for larger T_J (*Simion et al.* 2021). Across the range $2.0 \leq T_J \leq 2.8$, the asteroid to comet ratio settles to a steady mean value $\mathcal{R} = 6.2 \pm 0.8$, meaning that, in this T_J range, asteroids outnumber comets by ~6:1.

In the absence of main-belt contamination, $\mathcal{R}$ would give a measure of the ratio of the dynamical to the active cometary lifetimes. The measured $\mathcal{R} \sim 6$ would result if comets are active for only ~1/6th of their dynamical lifetimes. However, this is a lower limit because main-belt contamination is presumably non-zero. Furthermore, $\mathcal{R}$ provides no clue as to whether comets simply stop outgassing (because they exhaust near-surface volatiles), or cycle between active and inactive states (perhaps because of cyclic mantle build-up and blow-off correlated with changes in the perihelion distance and peak surface temperature; *Rickman et al.* 1990).

Dynamical simulations provide an independent perspective. The mean dynamical lifetime of JFCs is $\tau_d \sim 4 \times 10^5$ years (*Levison and Duncan* 1994). Repeated scattering by the terrestrial planets causes the mean inclination of the JFCs to increase with time. In order to reproduce the mod-

est inclinations of the JFCs (the mean and median values are 14.3° and 12.2°, respectively), these authors were forced to assume that the JFC physical lifetime is short compared to τ_d. Specifically, they inferred that the ratio of inactive to active JFCs should be in the range of 5 to 20, barely consistent with the measured $\mathcal{R} \sim 6$ for $2.0 \leq T_J \leq 2.8$.
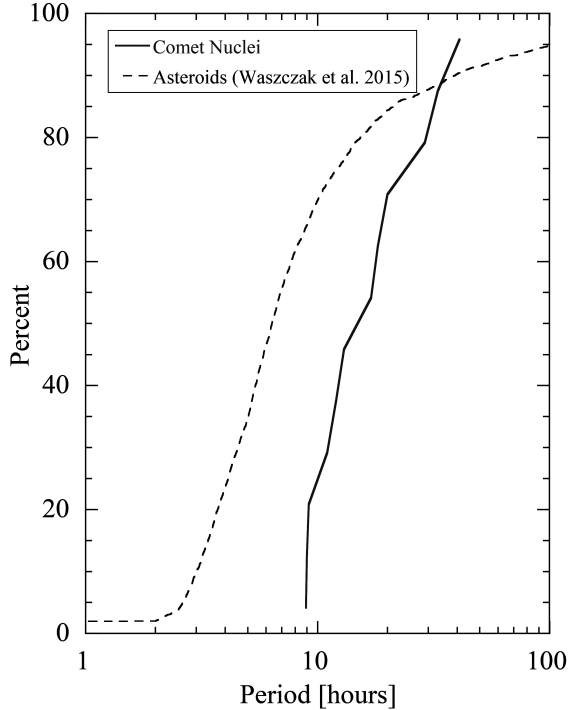

Fig. 19.— Comparison of the cumulative distributions of the rotation periods of JFCs (solid line) and asteroids (dashed line) in the 1 to 10 km size range. The much longer mean period of the JFCs is evident. From *Jewitt* (2021).

Another distinctive feature of JFC nuclei that might be helpful in the statistical identification of such objects when dormant is their rotation period distribution. The rotation periods of comets are highly biased towards long periods (median 15 hour) compared to the period distribution in small NEAs (median ~6 hour) (Figure 19; also see *Binzel et al.* 1992; *Jewitt* 2021). This difference, which likely reflects the lower bulk density of comets, where the critical period for rotational instability scales as $\rho^{-1/2}$ (Equation 8), would suggest that few ACOs are dead comets. Another pointer is the truncated size distribution and distinct lack of sub-km cometary nuclei compared to the high abundance of sub-km asteroids.

Table 2 shows that Damocloids (named after the prototype object (5335) Damocles; *Jewitt* 2005) are comparatively rare compared to comets with $T_J < 2$, accounting for only ~20% of the total ($\mathcal{R} = 0.2$) having $q < 2$ au. The ratio becomes even more extreme for smaller values of T_J. The Damocloid population grows larger when the
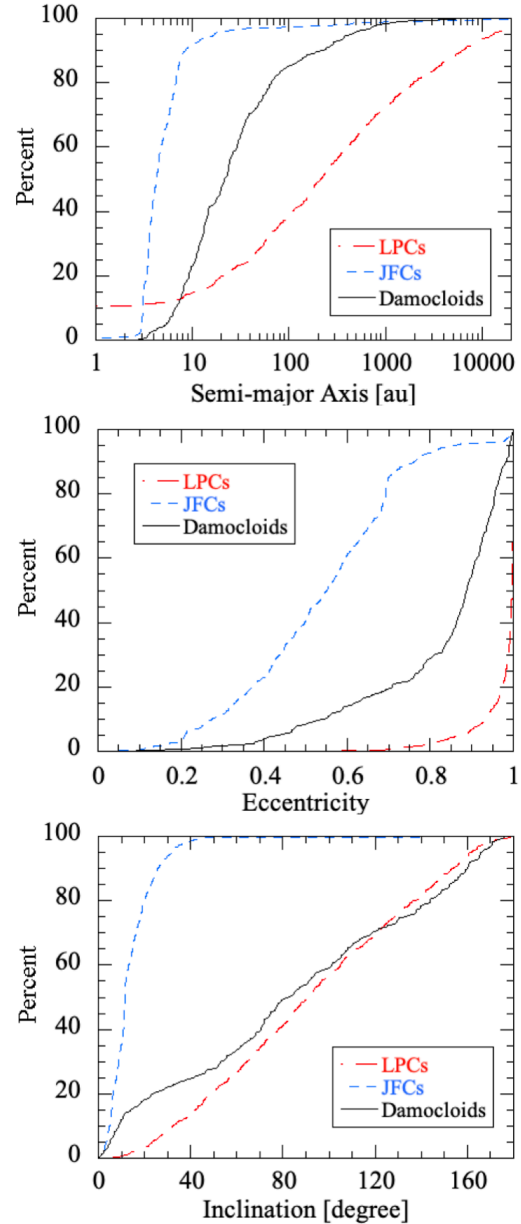

Fig. 20.— Comparison of the cumulative distributions of the orbital elements of Damocloids (solid black lines), JFCs (dashed blue lines), and LPCs (long-dashed red lines); (top) semi-major axis, (middle) eccentricity and (bottom) inclination. Compiled from JPL Horizons.

perihelion distance constraint in the table is relaxed, but this might just be because activity is harder to detect when $q \geq 2$ au. The table shows that, whereas apparent asteroids outnumber apparent comets in the range $2 \leq T_J \leq 3$, the opposite is true for $T_J < 2$. Currently 325 Damocloids are known, almost all of them reddish D-types (*Licandro et al.* 2018).

The orbital elements of Damocloids are compared with

those of JFCs and LPCs in Figure 20. In all three panels, the Damocloids are intermediate between the JFC and LPC populations. While the inclination distributions of Damocloids and LPCs are similar, albeit with a preponderance of prograde orbits in the former (median inclinations of $i = 73°$ for Damocloids vs. $i = 90°$ for the LPCs), the semimajor axis and eccentricity distributions are distinctly different. Therefore, we can reject the possibility that the Damocloids are exclusively dead or dormant LPC nuclei, and additional sources must be considered. *Wang et al.* (2012) suggest a combination of sources both in the Oort cloud and in the scattered disk component of the Kuiper belt. Numerical simulations show that transfer to and from the Scattered Disk population in the Kuiper belt can occur.

Several objects initially classified as Damocloids (e.g., C/2002 CE$_{10}$ (LINEAR) and C/2002 VQ$_{94}$ (LINEAR)) have subsequently been found to show activity. In some cases, the detection of coma simply reflects the acquisition of more sensitive measurements, but, in others, it appears that coma is intermittently present. These objects provide firm evidence that Damocloids and comets are compositionally as well as dynamically related.
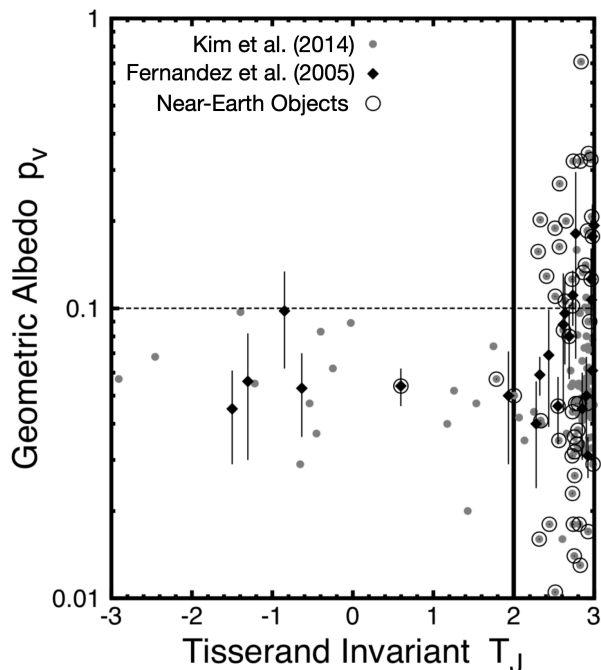

Fig. 21.— Albedo vs. Tisserand parameter. All objects with $T_J < 2$ have low (comet-like) albedos. From *Kim et al.* (2014).

An observational connection between dynamical and physical properties was established by *Fernández et al.* (2001), and confirmed by the addition of new measurements by *Fernández et al.* (2005) and *Kim et al.* (2014) (see Figure 21). Specifically, geometric albedos, p_V, are

observed to vary systematically with T_J, such that bodies with $T_J < 2$ have comet-like values $p_V = 0.05 \pm 0.02$, regardless of whether or not they show evidence for cometary activity, whereas bodies with $2 \leq T_J \leq 3$ show a wide range of albedos, particularly for $T_J \gtrsim 2.5$. *Kim et al.* (2014) emphasized the existence of high albedo ($p_V > 0.1$) objects in this population, similar to what is seen in the bona-fide asteroids ($T_J \geq 3$). The albedo trends in Figure 21 support the conclusions from Table 2, to the effect that Damocloids are mostly inactive comets while the ACO population consists of a mixture of (dark) inactive comets and (on average, brighter) bona-fide asteroids, though is dominated by the latter. Models indicate that objects can be scattered out of the protoplanetary disk by the giant planets from a wide range of initial orbits, even those interior to Jupiter (*Hahn and Malhotra* 1999). The systematically low (i.e., comet-like) albedos of Damocloids (Figure 21) indicate that such asteroidal bodies are uncommon.

LPCs showing weak evidence for activity are sometimes referred to as "Manx" objects, an allusion to the short-tailed mutant cats of the same name. It is not clear that the Manx objects are more than semantically different from weakly active LPCs; they could simply be low activity LPCs in which surface volatiles have been depleted in previous orbits. However, one object, C/2014 S3, shows a spectral continuum downturn near 1 μm similar to that seen in S-type asteroids (*Meech et al.* 2016). This might suggest the presence of more highly metamorphosed solids like those found in the S-type asteroids, with a possible origin nearer the Sun at higher temperatures than typical for the nuclei of LPCs. Unfortunately, it is not known whether the albedo of C/2014 S3 is like that of an S-type asteroid. Emplacement of objects formed inside the snow-line into the Oort cloud is inefficient because Jupiter scatters objects most efficiently to the interstellar medium, not the Oort cloud (*Hahn and Malhotra* 1999). *Shannon et al.* (2015) estimated that $\sim 8 \times 10^9$ asteroids could be so emplaced, which would comprise only $\sim$1% of the Oort cloud comet population ($\sim 10^{12}$ total objects). More 1 μm continuum spectra of long-period objects are needed to test any possible association with S-type or other inner-disk objects.

8. CENTAURS

Centaurs are generally considered to be an intermediate population of small bodies that are in dynamical transition from the trans-Neptunian population to the JFCs (see *Dones et al.* (2015) and the chapter by Fraser et al.) and thus are scientifically interesting as JFC precursors. Several working definitions of this population exist. Here, we refer to objects with both perihelia and semi-major axes in between the orbits of Jupiter (5.2 au) and Neptune (30 au) which are not in mean-motion resonances with the planets (e.g., excluding Jupiter and Neptune Trojans). The defining object in this class is 2060 Chiron ($a = 13.6$ au, $q = 8.5$ au),
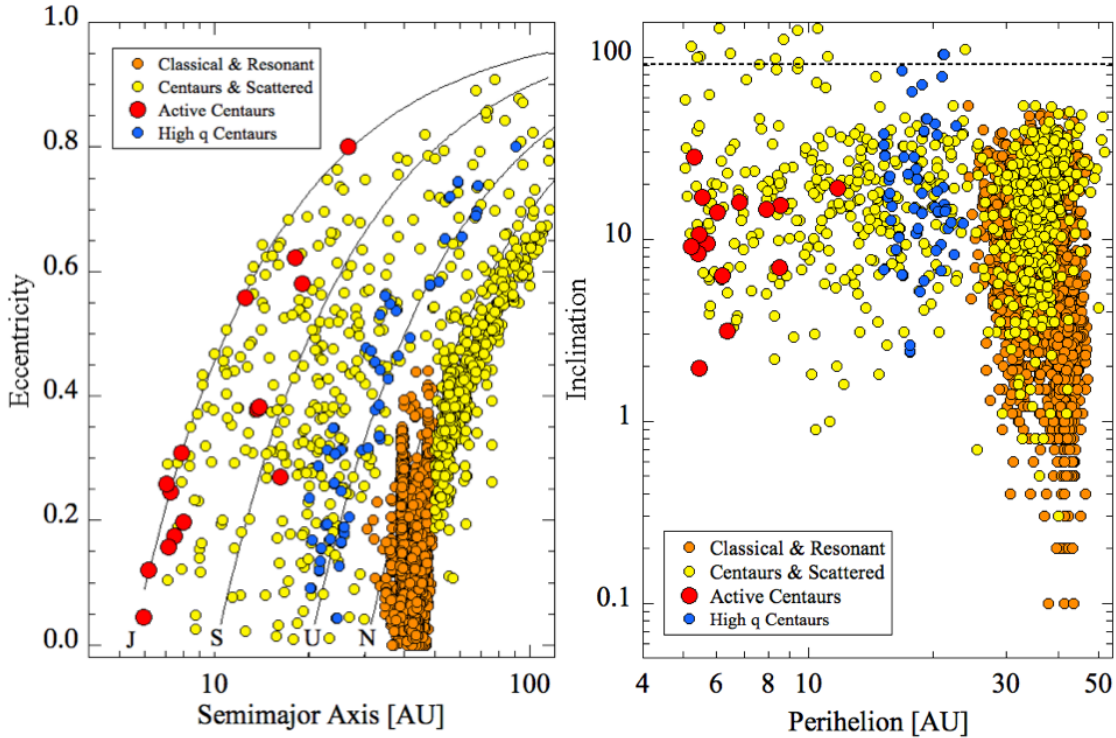
Fig. 22.— Orbital elements of outer solar system populations including the active (red) and inactive Centaurs. Semimajor axes of the major planets are marked J, S, U, and N. Diagonal arcs in the left panel show the loci of orbits having fixed perihelia, $q = a(1 - e)$, equal to the semi-major axes of the giant planets. The dotted horizontal line in the right panel is at $i = 90°$; objects above it are retrograde. The active Centaurs cluster within $q \lesssim 10$ au. Adapted from *Li et al.* (2020)

discovered in 1977 (*Kowal et al.* 1979), although comet 29P/Schwassmann-Wachmann 1, which has only recently come to be regarded as a Centaur, was actually discovered five decades before Chiron. About 430 Centaurs are known as of late 2021.

The Centaurs interact strongly with the giant planets and are consequently dynamically short-lived compared to the age of the solar system (*Horner et al.* 2004; *Volk and Malhotra* 2008). Centaur dynamical half-lives, $\tau_{1/2}$, are spread over a wide range, becoming shorter as the perihelion distance decreases, which is a reflection of the large mass and gravitational influence of Jupiter. *Horner et al.* (2004) bracketed the range of half-lives (expressed in Myr) as

$$0.39e^{0.135q} \lesssim \tau_{1/2} \lesssim 0.06e^{0.275Q} \qquad (13)$$

where q and Q are the perihelion and aphelion distances. Substituting q = 5.2 au and Q = 30 au, for example, gives $0.8 \lesssim \tau_{1/2} \lesssim 230$ Myr. Their source, at first unknown, is now firmly recognized as the Kuiper belt, specifically with the scattered disk component of the belt from which objects are destabilized by interactions with Neptune at perihelion (*Volk and Malhotra* 2008). The fate of the Centaurs, other than a few that collide with a giant planet, is either to be ejected from the solar system to interstellar space, or injected into the terrestrial planet region where they sublimate

and are re-labeled as JFCs *Levison and Duncan* (1994); *Sarid et al.* (2019). Unfortunately, the current orbit of any particular Centaur provides only a weak guide to its dynamical past because of the role of chaos induced by gas giant planet scattering. While there is a statistical flow of Centaurs from their source beyond 30 au inwards, the instantaneous orbit of an individual Centaur may be diffusing inwards or outwards at any given time.

About 31 of the known Centaurs have a cometary designation, corresponding to about 7% of the total. This is a lower limit to the true incidence of activity because most such objects have not been studied in detail sufficient to reveal activity even if it is present. Furthermore, most Centaur activity is transient, so that observations over a long period can only increase the estimated active fraction. Chiron itself shows intermittent mass loss, unconnected to its heliocentric distance.

Two properties distinguish active Centaurs from others (*Jewitt* 2009, 2015). First, their perihelia are preferentially small, typically $q \lesssim 8$ to 10 au (Figure 22, left panel). While observational selection does favor the detection of activity at small q, a sensitive, high resolution search for activity in 53 Centaurs with perihelia $q > 15$ au found none (*Li et al.* 2020). Second, while Centaurs as a whole show

a bimodal distribution of optical colors (*Peixinho et al.* 2012), this bimodality vanishes for objects with $q \lesssim 8$ to 10 au (c.f. Figure 22). The loss of bimodality occurs because the Centaurs lose ultrared matter, defined to have color index B-R > 1.6[4], and thought to consist of highly irradiated organics. The onset of activity and the disappearance of the ultrared matter appear to be correlated, in the sense that bodies which are active are rarely very red. Active centaur (523676) 2013 UL$_{10}$ with $B - R = 1.8 \pm 0.1$ is a possible exception (*Mazzotta Epifani et al.* 2018), although the colors are contradicted by *Tegler et al.* (2016), who measured $B - R = 1.62 \pm 0.03$ (plotted in Figure 23). This could mean that the ultrared matter, whose precise composition is unknown, is thermodynamically unstable at temperatures $\gtrsim 124$ K. Alternatively, a thin layer of ultrared matter could be ejected or simply buried by fallback debris excavated from beneath, as soon as the activity begins (*Jewitt* 2002). The smaller average perihelia of the active Centaurs correlate, as expected from Equation 13, with shorter mean dynamical lifetimes (*Melita and Licandro* 2012; *Fernández et al.* 2018).
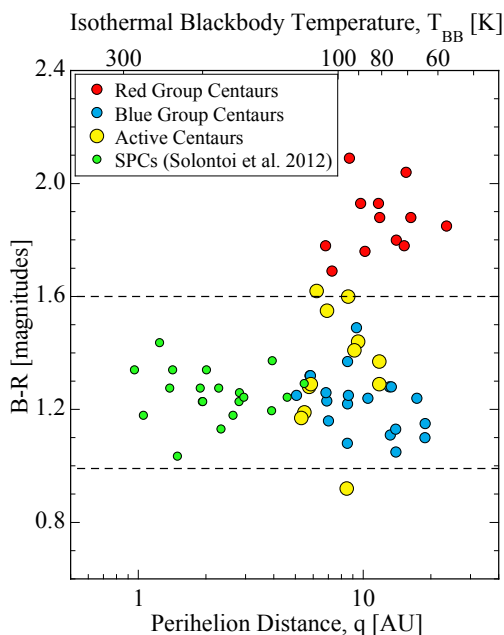

Fig. 23.— $B - R$ optical color as a function of perihelion distance for short-period comets (SPCs; synonymous here with JFCs) and active and inactive Centaurs, as marked. Horizontal dashed lines at $B - R = 0.99$ and $B - R = 1.6$ mark the colors of the Sun and the nominal beginning of the ultra-red objects, respectively. Adapted from *Jewitt* (2015).

What triggers Centaur activity near 8 to 10 au, where the isothermal blackbody temperature of a sphere is about 88 to 98 K? This is far too cold for water ice to sublimate. While water is not volatile enough, exposed supervolatile ices (e.g. CO) are too volatile, in the sense that they would easily drive activity at much larger distances than observed. For example, CO ice would sublimate strongly even at Kuiper belt distances and temperatures, where no activity is observed, and even CO_2 ice is in the strong-sublimation regime at distances ~ 10 au. Burial of super-volatile ices beneath a refractory mantle could, in principle, delay the onset of sublimation from an incoming body but would give no clear reason for a distinct turn-on distance at 8 to 10 au (c.f. Figure 22). Moreover, thermal evolution models suggest that *pure* CO cannot survive long-term in comets (*Davidsson* 2021). Explanations attempting to match activity to the sublimation of less volatile, less abundant materials (such as H_2S) struggle to provide a convincing match to the 8 to 10 au critical distance (*Poston et al.* 2018).

More promisingly, the crystallization timescale for amorphous water ice decreases exponentially with temperature, and first becomes less than the orbital period at ~ 10 au, suggesting that crystallization might drive Centaur activity (*Jewitt* 2009; *Guilbert-Lepoutre* 2012). Amorphous ice is the natural form of ice formed at low temperatures and gas pressures, so its incorporation in to the icy bodies of the outer solar system would not be surprising. Crystallization also fits the observed bursty nature of Centaur activity, corresponding to short-lived exothermic runaways in which trapped gases are expelled (see chapter by Prialnik and Jewitt). In addition, Centaur activity may be correlated with recent inward drift of the perihelion distance (*Fernández et al.* 2018), consistent with the crystallization hypothesis. Amorphous ice can trap CO, which has been reported in 29P/Schwassmann-Wachmann 1, (60558) Echeclus and 2060 Chiron (see review by *Womack et al.* 2017) but has not been detected in a majority of the Centaurs in which it has been sought (*Bockelée-Morvan et al.* 2001; *Jewitt et al.* 2008; *Drahus et al.* 2017). Absence of evidence is not necessarily evidence of absence, however, and the non-detections could simply reflect the difficulty in measuring CO rotational transitions in bodies far from the Earth. The onset of Centaur activity (Figure 22) and the collapse of the bimodal color distribution (Figure 23) are certainly consistent with an origin in the crystallization of amorphous ice, but it must be said that they do not prove that this is the responsible mechanism. Establishing proof of the existence of amorphous ice in JFCs and Centaurs would be of great scientific value. It would imply that ice in the precursor Kuiper belt objects has also survived in the amorphous state, significantly limiting the post-accretion thermal processing of these bodies (see Davidsson 2021 and the chapter by Prialnik and Jewitt).

---

[4]The color index B-R is defined as 2.5 times the logarithm of the ratio of the flux density measured in the R filter (center wavelength $\sim$6500Å) to that in the B filter (4500Å). Larger values indicate redder colors

9. FUTURE PROSPECTS AND CONCLUSIONS

Looking ahead, Rubin Observatory's Legacy Survey of Space and Time (LSST) should generate a massive temporal survey of the sky over 10 years and is expected to increase the numbers of known small solar system bodies in different populations by an order of magnitude or more (*Jones et al.* 2009; *Ivezić et al.* 2019). Its use of a 8.4 m-aperture telescope means that Rubin Observtory should achieve a sensitivity to faint activity that is unprecedented among wide-field surveys. Meanwhile, relevant upcoming NASA space-based observatories include the *Near-Earth Object Surveyor* (hereafter, *NEO Surveyor; Mainzer et al.* 2021), which aims to identify near-Earth objects that might present impact threats to Earth, and the Nancy Grace Roman Space Telescope (*Akeson et al.* 2019), which will conduct a wide-field survey that is nominally focused on dark energy and exoplanets, but which is expected to observe many solar system objects as well (although mostly at high ecliptic latitudes). Observing in the infrared, both spacecraft will be sensitive to thermal emission from long-lasting large dust grains ejected by active small bodies, potentially widening the observability window for detection of active events (e.g., *Holler et al.* 2018). In particular, *NEO Surveyor's* focus on discovering NEOs means that it should be able to greatly improve our understanding of the ratio of active and inactive small bodies in the terrestrial planet region. Taken together, these ever more sensitive searches for activity may reveal active objects in small body populations in which activity has yet to be found (e.g., the Jupiter Trojans) and will also provide a more thorough accounting of the extent of activity in populations already known to contain active objects like the NEOs, main-belt asteroids, and Centaurs, potentially allowing for further classification of active objects in those populations into smaller sub-groups based on physical or dynamical properties (e.g., *Hsieh and Haghighipour* 2016).

Continuing efforts to characterize individual active objects will also shed light on their physical nature, provide needed constraints for thermal models, and help to identify physically plausible activity mechanisms for each object. As most active events are of limited duration, sometimes lasting just a few days, useful characterization of new active objects discovered by LSST, *NEO Surveyor*, or the *Roman Space Telescope* will require rapid-response follow-up deep imaging and spectroscopy (e.g., *Najita et al.* 2016; *Street et al.* 2018). Long-term monitoring of known active objects (e.g., *Hsieh et al.* 2018a; *Wierzchos and Womack* 2020) is also needed to provide insights into both short-term and long-term activity evolution, while detailed characterization (e.g., measurements of phase functions, colors, and rotation states) of the nuclei of active objects during periods of inactivity (e.g., also see chapter by Knight et al.) provide information essential for thermal modeling studies (e.g. *Schörghofer et al.* 2020) and also constraining the properties of the population of other potentially active objects. Meanwhile, the recently launched *James Webb Space Telescope* and the upcoming generation of extremely large ($\sim$30 m-class) ground-based telescopes should enable searches for gas with unprecedented sensitivity (*Crampton and Simard* 2009; *Kelley et al.* 2016; *Wong et al.* 2020). Continued targeted and general dynamical studies investigating the connections between small body populations (see Section 5) will also be useful for identifying potential opportunities for close-proximity studies of active objects originally from the main asteroid belt (e.g., *Fernández et al.* 2017), much as classical comets give us the opportunity to study the composition of objects displaced from the outer solar system.

We can also look forward to a number of in-situ space missions currently being planned or proposed (also see chapter by Snodgrass et al.). The DESTINY+ spacecraft being developed by the Japan Aerospace Exploration Agency (JAXA) will visit Phaethon and has an expected launch date in 2024 (*Arai et al.* 2021). It will reach a close approach distance of 500 km from the object, briefly permitting imaging of the surface at $\leq$5 m pixel^{-1}, albeit at a flyby speed of 36 km s^{-1}. An impact ionization time-of-flight mass spectrometer will provide elemental compositions of any dust particles impacting the spacecraft, with a mass resolution of $M/\Delta M \sim$ 100 - 150 (*Krüger et al.* 2019). It should be noted, however, that the total dust mass that will be intercepted is modest: less than that of a single 30 μm particle (*Jewitt et al.* 2018a). Meanwhile, the Chinese National Space Agency's *ZhengHe* mission aims to visit active asteroid 311P, with an expected launch in 2025. Missions targeting MBCs have been proposed to both NASA and ESA (e.g., *Meech and Castillo-Rogez* 2015; *Jones et al.* 2018; *Snodgrass et al.* 2018), so far without success. In-situ studies are particularly needed to resolve major issues about the nature of MBC outgassing, because they provide the only means for investigating outgassed material with a mass spectrometer.

In terms of other interesting potential mission concepts, active asteroid 331P ejected $\sim$1% of its mass as recently as 2011, producing a debris trail and a chain of 19 or more fragments that grows in length at $\lesssim$10 cm s^{-1} (*Jewitt et al.* 2021). A single ion-driven spacecraft sent to this object could determine the (presumably) excited rotation state of the km-sized primary body, investigate the geology of the detachment scar at high resolution in order to assess the mode of failure, and then travel the length of the debris trail, visiting the $\sim$19 fragments one by one. The largest fragment, 331P-A, has an effective diameter of $\sim$200 m and shows a lightcurve consistent with a contact binary, presenting a particularly attractive target for in-situ investigation. Of course, we have already had one unexpected mission to an active asteroid, OSIRIS-REx's visit to Bennu. Because Bennu's activity was unexpected, only limited relevant observations were possible and the study of the ejected material has been inconclusive. Nevertheless, the discovery of

particles too large and sparse to be detected from Earth suggests that many other asteroids may be weakly active when examined closely, and that this possibility should be taken into account for future small body missions in general.

Our understanding of the asteroid-comet continuum has evolved substantially since the publication of Comets II (*Jewitt* 2004). We now recognize that many small bodies possess diverse combinations of physical and dynamical properties, and evolutionary histories, that cannot be cleanly associated with either asteroids or comets. Studies of extant volatile material from the inner portions of the protosolar disk are now possible, as are direct observations of asteroid collisions and rotational disruptions. New observations raise fresh questions about the incredible range of processes that can produce mass loss from small bodies and about the extent to which small bodies have been shuffled radially in the solar system since its formation. We anticipate even more exciting developments in the coming years.

REFERENCES

Agarwal J., Kim Y., Jewitt D. et al. (2020) *Component properties and mutual orbit of binary main-belt comet 288P/(300163) 2006 VW$_{139}$*, Astron. Astrophys., *643*, A152.

A'Hearn M. F., Belton M. J. S., Delamere A. et al. (2005) *Deep Impact: A Large-Scale Active Experiment on a Cometary Nucleus*, Space Sci. Rev., *117*, 1–21.

A'Hearn M. F., Millis R. C., Schleicher D. O. et al. (1995) *The ensemble properties of comets: Results from narrowband photometry of 85 comets, 1976-1992.*, Icarus, *118*, 223–270.

Akeson R., Armus L., Bachelet E. et al. (2019) *The Wide Field Infrared Survey Telescope: 100 Hubbles for the 2020s*, arXiv e-prints, arXiv:1902.05569.

Ansdell M., Meech K. J., Hainaut O. et al. (2014) *Refined Rotational Period, Pole Solution, and Shape Model for (3200) Phaethon*, Astrophys. J., *793*, 50.

Arai T., Yoshida F., Kobayashi M. et al. (2021) in *Lunar and Planetary Science Conference*, Lunar and Planetary Science Conference, p. 1896.

Arvidson R., Drozd R. J., Hohenberg C. M. et al. (1975) *Horizontal Transport of the Regolith, Modification of Features, and Erosion Rates on the Lunar Surface*, Moon, *13*, 67–79.

Babadzhanov P. B. (2003) *Meteor showers associated with the near-Earth asteroid (2101) Adonis*, Astron. Astrophys., *397*, 319–323.

Babadzhanov P. B., Kokhirova G. I., and Obrubov Y. V. (2015) *Extinct comets and asteroid-meteoroid complexes*, Solar System Research, *49*, 165–172.

Bach Y. P. and Ishiguro M. (2021) *Thermal radiation pressure as a possible mechanism for losing small particles on asteroids*, Astron. Astrophys., *654*, A113.

Bertini I. (2011) *Main Belt Comets: A new class of small bodies in the solar system*, Planet. Space Sci., *59*, 365–377.

Binzel R. P., Xu S., Bus S. J. et al. (1992) *Origins for the Near-Earth Asteroids*, Science, *257*, 779–782.

Birtwhistle P., Ryan W. H., Sato H. et al. (2010) *Comet P/2010 A2 (LINEAR)*, IAU Circ., *9105*.

Blaauw R. C. (2017) *The mass index and mass of the Geminid meteoroid stream as determined with radar, optical and lunar impact data*, Planet. Space Sci., *143*, 83–88.

Bockelée-Morvan D., Lellouch E., Biver N. et al. (2001) *Search for CO gas in Pluto, Centaurs and Kuiper Belt objects at radio wavelengths*, Astron. Astrophys., *377*, 343–353.

Bodewits D., Vincent J. B., and Kelley M. S. P. (2014) *Scheila's scar: Direct evidence of impact surface alteration on a primitive asteroid*, Icarus, *229*, 190–195.

Boehnhardt H., Schulz R., Tozzi G. P. et al. (1996) *Comet P/1996 N2 (Elst-Pizarro)*, IAU Circ., *6495*, 2.

Bose K. and Ganguly J. (1994) *Thermogravimetric study of the dehydration kinetics of talc*, American Mineralogist, *79*, 692–699.

Bottke W. F., Durda D. D., Nesvorný D. et al. (2005) *Linking the collisional history of the main asteroid belt to its dynamical excitation and depletion*, Icarus, *179*, 63–94.

Bottke W. F., Moorhead A. V., Connolly H. C. et al. (2020) *Meteoroid Impacts as a Source of Bennu's Particle Ejection Events*, Journal of Geophysical Research (Planets), *125*, e06282.

Bottke Jr. W. F., Vokrouhlický D., Rubincam D. P. et al. (2006) *The Yarkovsky and Yorp Effects: Implications for Asteroid Dynamics*, Annual Review of Earth and Planetary Sciences, *34*, 157–191.

Brasser R. and Wang J.-H. (2015) *An updated estimate of the number of Jupiter-family comets using a simple fading law*, Astron. Astrophys., *573*, A102.

Carusi A., Kresák Ľ., and Valsecchi G. B. (1995) *Conservation of the Tisserand Parameter at Close Encounters of Interplanetary Objects with Jupiter*, Earth Moon and Planets, *68*, 71–94.

Chandler C. O., Kueny J., Gustafsson A. et al. (2019) *Six Years of Sustained Activity in (6478) Gault*, Astrophys. J. Lett., *877*, L12.

Cikota S., Ortiz J. L., Cikota A. et al. (2014) *A photometric search for active Main Belt asteroids*, Astron. Astrophys., *562*, A94.

Colwell J. E., Gulbis A. A. S., Horányi M. et al. (2005) *Dust transport in photoelectron layers and the formation of dust ponds on Eros*, Icarus, *175*, 159–169.

Crampton D. and Simard L. (2009) *Solar System Capabilities of the Thirty Meter Telescope*, Earth Moon and Planets, *105*, 65–72.

Criswell D. R. (1973) in *Photon and Particle Interactions with Surfaces in Space* (R. J. L. Grard, ed.), vol. 37 of *Astrophysics and Space Science Library*, p. 545.

Criswell D. R. and De B. R. (1977) *Intense localized photoelectric charging in the lunar sunset terminator region, 2. Supercharging at the progression of sunset*, J. Geophys. Res., *82*, 1005.

Davidsson B. J. R. (2021) *Thermophysical evolution of planetesimals in the primordial disc*, Mon. Not. R. Astron. Soc., *505*, 5654–5685.

de León J., Campins H., Tsiganis K. et al. (2010) *Origin of the near-Earth asteroid Phaethon and the Geminids meteor shower*, Astron. Astrophys., *513*, A26.

DeMeo F. E., Alexander C. M. O., Walsh K. J. et al. (2015) *Asteroids IV*, pp. 13–41, Tucson, University of Arizona Press.

DeMeo F. E., Binzel R. P., Carry B. et al. (2014) *Unexpected D-*

type interlopers in the inner main belt, Icarus, *229*, 392–399.

DeMeo F. E. and Carry B. (2014) *Solar System evolution from compositional mapping of the asteroid belt*, Nature, *505*, 629–634.

Denneau L., Jedicke R., Fitzsimmons A. et al. (2015) *Observational constraints on the catastrophic disruption rate of small main belt asteroids*, Icarus, *245*, 1–15.

Devogèle M., Ferrais M., Jehin E. et al. (2021) *(6478) Gault: physical characterization of an active main-belt asteroid*, Mon. Not. R. Astron. Soc., *505*, 245–258.

Dones L., Brasser R., Kaib N. et al. (2015) *Origin and Evolution of the Cometary Reservoirs*, Space Sci. Rev., *197*, 191–269.

Drahus M., Waniak W., Tendulkar S. et al. (2015) *Fast Rotation and Trailing Fragments of the Active Asteroid P/2012 F5 (Gibbs)*, Astrophys. J. Lett., *802*, L8.

Drahus M., Yang B., Lis D. C. et al. (2017) *New Limits to CO Outgassing in Centaurs*, Mon. Not. R. Astron. Soc., *468*, 2897–2909.

Duncan M. J. (2008) *Dynamical Origin of Comets and Their Reservoirs*, Space Sci. Rev., *138*, 109–126.

Durech J., Vokrouhlický D., Pravec P. et al. (2018) *YORP and Yarkovsky effects in asteroids (1685) Toro, (2100) Ra-Shalom, (3103) Eger, and (161989) Cacus*, Astron. Astrophys., *609*, A86.

Durech J., Vokrouhlicky D., Pravec P. et al. (2022) *Rotation acceleration of asteroids (10115) 1992 SK, (1685) Toro, and (1620) Geographos due to the YORP effect*, Astron. Astrophys., *657*, A5.

Elst E. W., Pizarro O., Pollas C. et al. (1996) *Comet P/1996 N2 (Elst-Pizarro)*, IAU Circ., *6456*.

Encrenaz T. (2008) *Water in the solar system.*, Annu. Rev. Astron. Astrophys., *46*, 57–87.

Eppes M. C., Magi B., Hallet B. et al. (2016) *Deciphering the role of solar-induced thermal stresses in rock weathering*, GSA Bulletin, *128*, 1315–1338.

Fanale F. P. and Salvail J. R. (1989) *The water regime of asteroid (1) Ceres*, Icarus, *82*, 97–110.

Fernández J. A., Gallardo T., and Brunini A. (2002) *Are There Many Inactive Jupiter-Family Comets among the Near-Earth Asteroid Population?*, Icarus, *159*, 358–368.

Fernández J. A., Helal M., and Gallardo T. (2018) *Dynamical evolution and end states of active and inactive Centaurs*, Planet. Space Sci., *158*, 6–15.

Fernández J. A., Licandro J., Moreno F. et al. (2017) *Physical and dynamical properties of the anomalous comet 249P/LINEAR*, Icarus, *295*, 34–45.

Fernández J. A. and Sosa A. (2015) *Jupiter family comets in near-Earth orbits: Are some of them interlopers from the asteroid belt?*, Planet. Space Sci., *118*, 14–24.

Fernández Y. R., Jewitt D. C., and Sheppard S. S. (2001) *Low Albedos Among Extinct Comet Candidates*, Astrophys. J. Lett., *553*, L197–L200.

Fernández Y. R., Jewitt D. C., and Sheppard S. S. (2005) *Albedos of Asteroids in Comet-Like Orbits*, Astron. J., *130*, 308–318.

Fernández Y. R., McFadden L. A., Lisse C. M. et al. (1997) *Analysis of POSS Images of Comet-Asteroid Transition Object 107P/1949 W1 (Wilson-Harrington)*, Icarus, *128*, 114–126.

Ferrín I. and Orofino V. (2021) *Taurid complex smoking gun: Detection of cometary activity*, Planet. Space Sci., *207*, 105306.

Geem J., Ishiguro M., Bach Y. P. et al. (2021) *A polarimetric study of asteroids in comet-like orbits*, arXiv e-prints, arXiv:2111.00151.

Gilbert A. M. and Wiegert P. A. (2010) *Updated results of a search for main-belt comets using the Canada-France-Hawaii Telescope Legacy Survey*, Icarus, *210*, 998–999.

Gradie J. and Tedesco E. (1982) *Compositional Structure of the Asteroid Belt*, Science, *216*, 1405–1407.

Granvik M., Morbidelli A., Jedicke R. et al. (2016) *Super-catastrophic disruption of asteroids at small perihelion distances*, Nature, *530*, 303–306.

Guilbert-Lepoutre A. (2012) *Survival of Amorphous Water Ice on Centaurs*, Astron. J., *144*, 97.

Gundlach B. and Blum J. (2016) *Why are Jupiter-family comets active and asteroids in cometary-like orbits inactive?. How hydrostatic compression leads to inactivity*, Astron. Astrophys., *589*, A111.

Gustafson B. A. S. (1989) *Geminid meteoroids traced to cometary activity on Phaethon*, Astron. Astrophys., *225*, 533–540.

Haghighipour N., Maindl T. I., Schäfer C. et al. (2016) *Triggering Sublimation-driven Activity of Main Belt Comets*, Astrophys. J., *830*, 22.

Hahn J. M. and Malhotra R. (1999) *Orbital Evolution of Planets Embedded in a Planetesimal Disk*, Astron. J., *117*, 3041–3053.

Hainaut O. R., Kleyna J. T., Meech K. J. et al. (2019) *Disintegration of active asteroid P/2016 G1 (PANSTARRS)*, Astron. Astrophys., *628*, A48.

Hanuš J., Delbo' M., Vokrouhlický D. et al. (2016) *Near-Earth asteroid (3200) Phaethon: Characterization of its orbit, spin state, and thermophysical parameters*, Astron. Astrophys., *592*, A34.

Harris A. W., Fahnestock E. G., and Pravec P. (2009) *On the shapes and spins of "rubble pile" asteroids*, Icarus, *199*, 310–318.

Harsono D., Bruderer S., and van Dishoeck E. F. (2015) *Volatile snowlines in embedded disks around low-mass protostars*, Astron. Astrophys., *582*, A41.

Hartmann W. K., Tholen D. J., Meech K. J. et al. (1990) *2060 Chiron: Colorimetry and cometary behavior*, Icarus, *83*, 1–15.

Hasegawa S., Marsset M., DeMeo F. E. et al. (2021a) *Discovery of Two TNO-like Bodies in the Asteroid Belt*, Astrophys. J. Lett., *916*, L6.

Hasegawa S., Marsset M., DeMeo F. E. et al. (2021b) *The appearance of a 'fresh' surface on 596 Scheila as a consequence of the 2010 impact event*, arXiv e-prints, arXiv:2112.04672.

Heiken G. H., Vaniman D. T., and French B. M. (1991) *Lunar Sourcebook, A User's Guide to the Moon*.

Hergenrother C. W., Maleszewski C., Li J. Y. et al. (2020) *Photometry of Particles Ejected From Active Asteroid (101955) Bennu*, Journal of Geophysical Research (Planets), *125*, e06381.

Hirabayashi M., Sánchez D. P., and Scheeres D. J. (2015) *Internal Structure of Asteroids Having Surface Shedding Due to Rotational Instability*, Astrophys. J., *808*, 63.

Hirabayashi M., Scheeres D. J., Sánchez D. P. et al. (2014) *Constraints on the Physical Properties of Main Belt Comet P/2013 R3 from its Breakup Event*, Astrophys. J. Lett., *789*, L12.

Holler B. J., Milam S. N., Bauer J. M. et al. (2018) *Solar system science with the Wide-Field Infrared Survey Telescope*, Journal of Astronomical Telescopes, Instruments, and Systems, *4*, 034003.

Holsapple K. A. and Housen K. R. (2019) *The catastrophic disruptions of asteroids: History, features, new constraints and interpretations*, Planet. Space Sci., *179*, 104724.

Hood N., Carroll A., Wang X. et al. (2022) *Laboratory measurements of size distribution of electrostatically lofted dust*,

Icarus, *371*, 114684.

Horner J., Evans N. W., and Bailey M. E. (2004) *Simulations of the population of Centaurs - I. The bulk statistics*, *Mon. Not. R. Astron. Soc.*, *354*, 798–810.

Horz F. and Cintala M. (1997) *Impact experiments related to the evolution of planetary regoliths*, *Meteorit. Planet. Sci.*, *32*, 179–209.

Housen K. R., Sweet W. J., and Holsapple K. A. (2018) *Impacts into porous asteroids*, *Icarus*, *300*, 72–96.

Hsieh H. H. (2009) *The Hawaii trails project: comet-hunting in the main asteroid belt*, *Astron. Astrophys.*, *505*, 1297–1310.

Hsieh H. H. (2014a) in *IAU Symposium: Formation, Detection, and Characterization of Extrasolar Habitable Planets*, vol. 293 of *IAU Symposium*, pp. 212–218.

Hsieh H. H. (2014b) *The nucleus of main-belt Comet P/2010 R2 (La Sagra)*, *Icarus*, *243*, 16–26.

Hsieh H. H. (2017) *Asteroid-comet continuum objects in the solar system*, *Philosophical Transactions of the Royal Society of London Series A*, *375*, 20160259.

Hsieh H. H., Chandler C. O., Denneau L. et al. (2021a) *Physical Characterization of Main-belt Comet (248370) 2005 QN$_{173}$*, *Astrophys. J. Lett.*, *922*, L9.

Hsieh H. H., Denneau L., Wainscoat R. J. et al. (2015a) *The main-belt comets: The Pan-STARRS1 perspective*, *Icarus*, *248*, 289–312.

Hsieh H. H. and Haghighipour N. (2016) *Potential Jupiter-Family comet contamination of the main asteroid belt*, *Icarus*, *277*, 19–38.

Hsieh H. H., Hainaut O., Novaković B. et al. (2015b) *Sublimation-Driven Activity in Main-Belt Comet 313p/Gibbs*, *Astrophys. J. Lett.*, *800*, L16.

Hsieh H. H., Ishiguro M., Kim Y. et al. (2018a) *The 2016 Reactivations of the Main-belt Comets 238P/Read and 288P/(300163) 2006 VW$_{139}$*, *Astron. J.*, *156*, 223.

Hsieh H. H., Ishiguro M., Knight M. M. et al. (2018b) *The Reactivation and Nucleus Characterization of Main-belt Comet 358P/PANSTARRS (P/2012 T1)*, *Astron. J.*, *156*, 39.

Hsieh H. H., Ishiguro M., Knight M. M. et al. (2021b) *The Reactivation of Main-belt Comet 259P/Garradd (P/2008 R1)*, *Planet. Sci. J.*, *2*, 62.

Hsieh H. H., Ishiguro M., Lacerda P. et al. (2011a) *Physical Properties of Main-belt Comet 176P/LINEAR*, *Astron. J.*, *142*, 29.

Hsieh H. H. and Jewitt D. (2005) *Search for Activity in 3200 Phaethon*, *Astrophys. J.*, *624*, 1093–1096.

Hsieh H. H. and Jewitt D. (2006) *A Population of Comets in the Main Asteroid Belt*, *Science*, *312*, 561–563.

Hsieh H. H., Jewitt D., and Fernández Y. R. (2009a) *Albedos of Main-Belt Comets 133P/Elst-Pizarro and 176P/LINEAR*, *Astrophys. J. Lett.*, *694*, L111–L114.

Hsieh H. H., Jewitt D., and Ishiguro M. (2009b) *Physical Properties of Main-Belt Comet P/2005 U1 (Read)*, *Astron. J.*, *137*, 157–168.

Hsieh H. H., Jewitt D., Lacerda P. et al. (2010) *The return of activity in main-belt comet 133P/Elst-Pizarro*, *Mon. Not. R. Astron. Soc.*, *403*, 363–377.

Hsieh H. H., Jewitt D. C., and Fernández Y. R. (2004) *The Strange Case of 133P/Elst-Pizarro: A Comet among the Asteroids*, *Astron. J.*, *127*, 2997–3017.

Hsieh H. H., Kaluna H. M., Novaković B. et al. (2013) *Main-belt Comet P/2012 T1 (PANSTARRS)*, *Astrophys. J. Lett.*, *771*, L1.

Hsieh H. H., Meech K. J., and Pittichová J. (2011b) *Main-belt Comet 238P/Read Revisited*, *Astrophys. J. Lett.*, *736*, L18.

Hsieh H. H., Novaković B., Kim Y. et al. (2018c) *Asteroid Family Associations of Active Asteroids*, *Astron. J.*, *155*, 96.

Hsieh H. H., Novaković B., Walsh K. J. et al. (2020) *Potential Themis-family Asteroid Contribution to the Jupiter-family Comet Population*, *Astron. J.*, *159*, 179.

Hsieh H. H. and Sheppard S. S. (2015) *The reactivation of main-belt Comet 324P/La Sagra (P/2010 R2)*, *Mon. Not. R. Astron. Soc.*, *454*, L81–L85.

Hsieh H. H., Yang B., and Haghighipour N. (2012a) *Optical and Dynamical Characterization of Comet-like Main-belt Asteroid (596) Scheila*, *Astrophys. J.*, *744*, 9.

Hsieh H. H., Yang B., Haghighipour N. et al. (2012b) *Discovery of Main-belt Comet P/2006 VW$_{139}$ by Pan-STARRS1*, *Astrophys. J. Lett.*, *748*, L15.

Hsieh H. H., Yang B., Haghighipour N. et al. (2012c) *Observational and Dynamical Characterization of Main-belt Comet P/2010 R2 (La Sagra)*, *Astron. J.*, *143*, 104.

Hui M.-T. and Jewitt D. (2017) *Non-gravitational Acceleration of the Active Asteroids*, *Astron. J.*, *153*, 80.

Hui M.-T., Jewitt D., and Du X. (2017) *Split Active Asteroid P/2016 J1 (PANSTARRS)*, *Astron. J.*, *153*, 141.

Hui M.-T. and Li J. (2017) *Resurrection of (3200) Phaethon in 2016*, *Astron. J.*, *153*, 23.

Ishiguro M., Hanayama H., Hasegawa S. et al. (2011a) *Interpretation of (596) Scheila's Triple Dust Tails*, *Astrophys. J. Lett.*, *741*, L24.

Ishiguro M., Hanayama H., Hasegawa S. et al. (2011b) *Observational Evidence for an Impact on the Main-belt Asteroid (596) Scheila*, *Astrophys. J. Lett.*, *740*, L11.

Ishiguro M., Sarugaku Y., Nishihara S. et al. (2009) *Report on the Kiso cometary dust trail survey*, *Advances in Space Research*, *43*, 875–879.

Ivezić Ž., Kahn S. M., Tyson J. A. et al. (2019) *LSST: From Science Drivers to Reference Design and Anticipated Data Products*, *Astrophys. J.*, *873*, 111.

Izidoro A., de Souza Torres K., Winter O. C. et al. (2013) *A Compound Model for the Origin of Earth's Water*, *Astrophys. J.*, *767*, 54.

Jenniskens P. (2008) *Meteor Showers and their Parent Comets*, Cambridge, UK: Cambridge University Press.

Jenniskens P. (2015) *Meteoroid Streams and the Zodiacal Cloud*, pp. 281–295, Tucson, University of Arizona Press.

Jewitt D. (1996) *From Comets to Asteroids: When Hairy Stars Go Bald*, *Earth Moon and Planets*, *72*, 185–201.

Jewitt D. (2002) *From Kuiper Belt Object to Cometary Nucleus: The Missing Ultrared Matter*, *Astron. J.*, *123*, 1039–1049.

Jewitt D. (2004) *From cradle to grave: the rise and demise of the comets*, p. 659, Tucson, University of Arizona Press.

Jewitt D. (2005) *A First Look at the Damocloids*, *Astron. J.*, *129*, 530–538.

Jewitt D. (2009) *The Active Centaurs*, *Astron. J.*, *137*, 4296–4312.

Jewitt D. (2012) *The Active Asteroids*, *Astron. J.*, *143*, 66.

Jewitt D. (2015) *Color Systematics of Comets and Related Bodies*, *Astron. J.*, *150*, 201.

Jewitt D. (2020) *138175 (2000 EE104) and the Source of Interplanetary Field Enhancements*, *Planet. Sci. J.*, *1*, 33.

Jewitt D. (2021) *Systematics and Consequences of Comet Nucleus Outgassing Torques*, *Astron. J.*, *161*, 261.

Jewitt D., Agarwal J., Li J. et al. (2014a) *Disintegrating Asteroid P/2013 R3*, *Astrophys. J. Lett.*, *784*, L8.

Jewitt D., Agarwal J., Li J. et al. (2017) *Anatomy of an Asteroid Breakup: The Case of P/2013 R3*, *Astron. J.*, *153*, 223.

Jewitt D., Agarwal J., Weaver H. et al. (2013a) *The Extraordinary Multi-tailed Main-belt Comet P/2013 P5*, *Astrophys. J. Lett.*, *778*, L21.

Jewitt D., Asmus D., Yang B. et al. (2019a) *High-resolution Thermal Infrared Imaging of 3200 Phaethon*, *Astron. J.*, *157*, 193.

Jewitt D., Garland C. A., and Aussel H. (2008) *Deep Search for Carbon Monoxide in Cometary Precursors Using Millimeter Wave Spectroscopy*, *Astron. J.*, *135*, 400–407.

Jewitt D. and Hsieh H. (2006) *Physical Observations of 2005 UD: A Mini-Phaethon*, *Astron. J.*, *132*, 1624–1629.

Jewitt D., Hsieh H., and Agarwal J. (2015) *Asteroids IV*, pp. 221–241, Tucson, University of Arizona Press.

Jewitt D., Ishiguro M., Weaver H. et al. (2014b) *Hubble Space Telescope Investigation of Main-belt Comet 133P/Elst-Pizarro*, *Astron. J.*, *147*, 117.

Jewitt D., Kim Y., Luu J. et al. (2019b) *Episodically Active Asteroid 6478 Gault*, *Astrophys. J. Lett.*, *876*, L19.

Jewitt D., Kim Y., Rajagopal J. et al. (2019c) *Active Asteroid P/2017 S5 (ATLAS)*, *Astron. J.*, *157*, 54.

Jewitt D. and Li J. (2010) *Activity in Geminid Parent (3200) Phaethon*, *Astron. J.*, *140*, 1519–1527.

Jewitt D., Li J., and Agarwal J. (2013b) *The Dust Tail of Asteroid (3200) Phaethon*, *Astrophys. J. Lett.*, *771*, L36.

Jewitt D., Li J., and Kim Y. (2021) *Fragmenting Active Asteroid 331P/Gibbs*, *Astron. J.*, *162*, 268.

Jewitt D., Mutchler M., Agarwal J. et al. (2018a) *Hubble Space Telescope Observations of 3200 Phaethon at Closest Approach*, *Astron. J.*, *156*, 238.

Jewitt D., Stuart J. S., and Li J. (2011a) *Pre-discovery Observations of Disrupting Asteroid P/2010 A2*, *Astron. J.*, *142*, 28.

Jewitt D., Weaver H., Agarwal J. et al. (2010a) *A recent disruption of the main-belt asteroid P/2010A2*, *Nature*, *467*, 817–819.

Jewitt D., Weaver H., Agarwal J. et al. (2010b) *A recent disruption of the main-belt asteroid P/2010A2*, *Nature*, *467*, 817–819.

Jewitt D., Weaver H., Mutchler M. et al. (2011b) *Hubble Space Telescope Observations of Main-belt Comet (596) Scheila*, *Astrophys. J. Lett.*, *733*, L4.

Jewitt D., Weaver H., Mutchler M. et al. (2018b) *The Nucleus of Active Asteroid 311P/(2013 P5) PANSTARRS*, *Astron. J.*, *155*, 231.

Jones G. H., Agarwal J., Bowles N. et al. (2018) *The proposed Caroline ESA M3 mission to a Main Belt Comet*, *Advances in Space Research*, *62*, 1921–1946.

Jones G. H., Balogh A., Russell C. T. et al. (2003) *Possible Distortion of the Interplanetary Magnetic Field by the Dust Trail of Comet 122P/de Vico*, *Astrophys. J. Lett.*, *597*, L61–L64.

Jones R. L., Chesley S. R., Connolly A. J. et al. (2009) *Solar System Science with LSST*, *Earth Moon and Planets*, *105*, 101–105.

Jones T. D., Lebofsky L. A., Lewis J. S. et al. (1990) *The composition and origin of the C, P, and D asteroids: Water as a tracer of thermal evolution in the outer belt*, *Icarus*, *88*, 172–192.

Jutzi M., Holsapple K., Wünneman K. et al. (2015) *Asteroids IV*, pp. 679–699, Tucson, University of Arizona Press.

Kańuchová Z. and Neslušan L. (2007) *The parent bodies of the Quadrantid meteoroid stream*, *Astron. Astrophys.*, *470*, 1123–1136.

Kareta T., Reddy V., Pearson N. et al. (2021) *Investigating the Relationship between (3200) Phaethon and (155140) 2005 UD through Telescopic and Laboratory Studies*, *arXiv e-prints*, arXiv:2109.01020.

Kasuga T. and Jewitt D. (2008) *Observations of 1999 YC and the Breakup of the Geminid Stream Parent*, *Astron. J.*, *136*, 881–889.

Kasuga T. and Jewitt D. (2019) *Asteroid-Meteoroid Complexes*, p. 187, Cambridge, UK, Cambridge University Press.

Kelley M. S. P., Woodward C. E., Bodewits D. et al. (2016) *Cometary Science with the James Webb Space Telescope*, *PASP*, *128*, 018009.

Kim Y., Agarwal J., Jewitt D. et al. (2019) in *EPSC-DPS Joint Meeting 2019*, vol. 2019, pp. EPSC–DPS2019–986.

Kim Y., Ishiguro M., and Lee M. G. (2017a) *New Observational Evidence of Active Asteroid P/2010 A2: Slow Rotation of the Largest Fragment*, *Astrophys. J. Lett.*, *842*, L23.

Kim Y., Ishiguro M., Michikami T. et al. (2017b) *Anisotropic Ejection from Active Asteroid P/2010 A2: An Implication of Impact Shattering on an Asteroid*, *Astron. J.*, *153*, 228.

Kim Y., Ishiguro M., and Usui F. (2014) *Physical Properties of Asteroids in Comet-like Orbits in Infrared Asteroid Survey Catalogs*, *Astrophys. J.*, *789*, 151.

Kim Y., JeongAhn Y., and Hsieh H. H. (2018) *Orbital Alignment of Main-belt Comets*, *Astron. J.*, *155*, 142.

Kleyna J. T., Hainaut O. R., and Meech K. (2019) *The Sporadic Activity of (6478) Gault: A YORP-driven Event?*, *Astrophys. J. Lett.*, *874*, L20.

Konietzky H. and Wang F. (1992) *Chapter iv. thermal expansion of rocks*, *Developments in Petroleum Science Thermal properties and temperature-related behavior of rock/fluid systems*, p. 29–38.

Kowal C. T., Liller W., and Marsden B. G. (1979) in *Dynamics of the Solar System* (R. L. Duncombe, ed.), vol. 81, p. 245.

Krüger H., Strub P., Srama R. et al. (2019) *Modelling DESTINY$^+$ interplanetary and interstellar dust measurements en route to the active asteroid (3200) Phaethon*, *Planet. Space Sci.*, *172*, 22–42.

Küppers M., O'Rourke L., Bockelée-Morvan D. et al. (2014) *Localized sources of water vapour on the dwarf planet (1) Ceres*, *Nature*, *505*, 525–527.

Lai H. R., Russell C. T., Wei H. Y. et al. (2017) *Possible potentially threatening co-orbiting material of asteroid 2000EE104 identified through interplanetary magnetic field disturbances*, *Meteorit. Planet. Sci.*, *52*, 1125–1132.

Larson S. M. (2010) *(596) Scheila*, *IAU Circ.*, *9188*, 1.

Lauretta D. S., Hergenrother C. W., Chesley S. R. et al. (2019) *Episodes of particle ejection from the surface of the active asteroid (101955) Bennu*, *Science*, *366*, 3544.

Lee H.-J., Ďurech J., Vokrouhlický D. et al. (2021) *Spin Change of Asteroid 2012 TC4 Probably by Radiation Torques*, *Astron. J.*, *161*, 112.

Levison H. F. (1996) in *Completing the Inventory of the Solar System* (T. Rettig and J. M. Hahn, eds.), vol. 107 of *Astronomical Society of the Pacific Conference Series*, pp. 173–191.

Levison H. F., Bottke W. F., Gounelle M. et al. (2009) *Contamination of the asteroid belt by primordial trans-Neptunian objects*, *Nature*, *460*, 364–366.

Levison H. F. and Duncan M. J. (1994) *The Long-Term Dynamical Behavior of Short-Period Comets*, *Icarus*, *108*, 18–36.

Levison H. F., Terrell D., Wiegert P. A. et al. (2006) *On the origin of the unusual orbit of Comet 2P/Encke*, *Icarus*, *182*, 161–168.

Li J. and Jewitt D. (2013) *Recurrent Perihelion Activity in (3200) Phaethon*, *Astron. J.*, *145*, 154.

Li J., Jewitt D., Mutchler M. et al. (2020) *Hubble Space Telescope Search for Activity in High-perihelion Objects*, *Astron. J.*, *159*, 209.

Licandro J., Alvarez-Candal A., de León J. et al. (2008) *Spectral properties of asteroids in cometary orbits*, Astron. Astrophys., *481*, 861–877.

Licandro J., Campins H., Kelley M. et al. (2009) *Spitzer observations of the asteroid-comet transition object and potential spacecraft target 107P (4015) Wilson-Harrington*, Astron. Astrophys., *507*, 1667–1670.

Licandro J., Popescu M., de León J. et al. (2018) *The visible and near-infrared spectra of asteroids in cometary orbits*, Astron. Astrophys., *618*, A170.

Lichtenberg T., Drążkowska J., Schönbächler M. et al. (2021) *Bifurcation of planetary building blocks during Solar System formation*, Science, *371*, 365–370.

Lowry S. C., Weissman P. R., Duddy S. R. et al. (2014) *The internal structure of asteroid (25143) Itokawa as revealed by detection of YORP spin-up*, Astron. Astrophys., *562*, A48.

Luu J. X. and Jewitt D. C. (1990) *Cometary Activity in 2060 Chiron*, Astron. J., *100*, 913.

Luu J. X., Jewitt D. C., Mutchler M. et al. (2021) *Rotational Mass Shedding from Asteroid (6478) Gault*, Astrophys. J. Lett., *910*, L27.

MacLennan E., Toliou A., and Granvik M. (2021) *Dynamical evolution and thermal history of asteroids (3200) Phaethon and (155140) 2005 UD*, Icarus, *366*, 114535.

MacLennan E. M. and Hsieh H. H. (2012) *The Nucleus of Mainbelt Comet 259P/Garradd*, Astrophys. J. Lett., *758*, L3.

Mainzer A., Abell P., Bauer J. et al. (2021) in *AAS/Division for Planetary Sciences Meeting Abstracts*, vol. 53, p. 306.16.

Mainzer A., Read M. T., Scottii J. V. et al. (2010) *Comet P/2009 WJ_50 (La Sagra).*, IAU Circ., *9117*.

Mann I. (2017) *Comets as a possible source of nanodust in the Solar System cloud and in planetary debris discs*, Philosophical Transactions of the Royal Society of London Series A, *375*, 20160254.

Marchi S., Chapman C. R., Barnouin O. S. et al. (2015) *Asteroids IV*, pp. 725–744, Tucson, University of Arizona Press.

Martin R. G. and Livio M. (2012) *On the evolution of the snow line in protoplanetary discs*, Mon. Not. R. Astron. Soc., *425*, L6–L9.

Marzari F., Rossi A., and Scheeres D. J. (2011) *Combined effect of YORP and collisions on the rotation rate of small Main Belt asteroids*, Icarus, *214*, 622–631.

Masiero J. R., Davidsson B. J. R., Liu Y. et al. (2021) *Volatility of Sodium in Carbonaceous Chondrites at Temperatures Consistent with Low-perihelion Asteroids*, Planet. Sci. J., *2*, 165.

Mazzotta Epifani E., Dotto E., Ieva S. et al. (2018) *523676 (2013 UL10): the first active red centaur*, Astron. Astrophys., *620*, A93.

McLoughlin E., Fitzsimmons A., and McLoughlin A. (2015) *Modelling the brightness increase signature due to asteroid collisions*, Icarus, *256*, 37–48.

Meech K. J. and Belton M. J. S. (1990) *The Atmosphere of 2060 Chiron*, Astron. J., *100*, 1323.

Meech K. J. and Castillo-Rogez J. C. (2015) in *IAU General Assembly*, vol. 29, p. 2257859.

Meech K. J., Yang B., Kleyna J. et al. (2016) *Inner solar system material discovered in the Oort cloud*, Science Advances, *2*, e1600038.

Melita M. D. and Licandro J. (2012) *Links between the dynamical evolution and the surface color of the Centaurs*, Astron. Astrophys., *539*, A144.

Michel P., Ballouz R. L., Barnouin O. S. et al. (2020) *Collisional formation of top-shaped asteroids and implications for the origins of Ryugu and Bennu*, Nature Communications, *11*, 2655.

Molaro J. L., Byrne S., and Langer S. A. (2015) *Grain-scale thermoelastic stresses and spatiotemporal temperature gradients on airless bodies, implications for rock breakdown*, Journal of Geophysical Research (Planets), *120*, 255–277.

Molaro J. L., Hergenrother C. W., Chesley S. R. et al. (2020) *Thermal Fatigue as a Driving Mechanism for Activity on Asteroid Bennu*, Journal of Geophysical Research (Planets), *125*, e06325.

Mommert M., Hora J. L., Harris A. W. et al. (2014) *The Discovery of Cometary Activity in Near-Earth Asteroid (3552) Don Quixote*, Astrophys. J., *781*, 25.

Moreno F., Licandro J., Cabrera-Lavers A. et al. (2021) *Dust environment of active asteroids P/2019 A4 (PANSTARRS) and P/2021 A5 (PANSTARRS)*, Mon. Not. R. Astron. Soc., *506*, 1733–1740.

Moreno F., Licandro J., Cabrera-Lavers A. et al. (2016a) *Dust Loss from Activated Asteroid P/2015 X6*, Astrophys. J., *826*, 137.

Moreno F., Licandro J., Cabrera-Lavers A. et al. (2016b) *Early Evolution of Disrupted Asteroid P/2016 G1 (PANSTARRS)*, Astrophys. J. Lett., *826*, L22.

Moreno F., Pozuelos F. J., Novaković B. et al. (2017) *The Splitting of Double-component Active Asteroid P/2016 J1 (PANSTARRS)*, Astrophys. J. Lett., *837*, L3.

Murray C. D. and Dermott S. F. (2000) *Solar System Dynamics*, Cambridge University Press.

Najita J., Willman B., Finkbeiner D. P. et al. (2016) *Maximizing Science in the Era of LSST: A Community-Based Study of Needed US Capabilities*, arXiv e-prints, arXiv:1610.01661.

Nakano R. and Hirabayashi M. (2020) *Mass-shedding Activities of Asteroid (3200) Phaethon Enhanced by Its Rotation*, Astrophys. J. Lett., *892*, L22.

Nesvorný D., Bottke W. F., Vokrouhlický D. et al. (2008) *Origin of the Near-Ecliptic Circumsolar Dust Band*, Astrophys. J. Lett., *679*, L143-L146.

Nesvorný D., Brož M., and Carruba V. (2015) *Asteroids IV*, pp. 297–321, Tucson, University of Arizona Press.

Nesvorný D., Janches D., Vokrouhlický D. et al. (2011) *Dynamical Model for the Zodiacal Cloud and Sporadic Meteors*, Astrophys. J., *743*, 129.

Novaković B., Hsieh H. H., and Cellino A. (2012) *P/2006 VW$_{139}$: a main-belt comet born in an asteroid collision?*, Mon. Not. R. Astron. Soc., *424*, 1432–1441.

Ohtsuka K., Sekiguchi T., Kinoshita D. et al. (2006) *Apollo asteroid 2005 UD: split nucleus of (3200) Phaethon?*, Astron. Astrophys., *450*, L25–L28.

Ostro S. J., Margot J.-L., Benner L. A. M. et al. (2006) *Radar Imaging of Binary Near-Earth Asteroid (66391) 1999 KW4*, Science, *314*, 1276–1280.

Park R. S., Konopliv A. S., Bills B. G. et al. (2016) *A partially differentiated interior for (1) Ceres deduced from its gravity field and shape*, Nature, *537*, 515–517.

Peixinho N., Delsanti A., Guilbert-Lepoutre A. et al. (2012) *The bimodal colors of Centaurs and small Kuiper belt objects*, Astron. Astrophys., *546*, A86.

Piro C., Meech K. J., Bufanda E. et al. (2021) *Characterizing the Manx Candidate A/2018 V3*, Planet. Sci. J., *2*, 33.

Podolak M. and Herman G. (1985) *Numerical simulations of comet nuclei II. The effect of the dust mantle*, Icarus, *61*, 267–277.

Poston M. J., Mahjoub A., Ehlmann B. L. et al. (2018) *Visible*

Near-infrared Spectral Evolution of Irradiated Mixed Ices and Application to Kuiper Belt Objects and Jupiter Trojans, *Astrophys. J.*, *856*, 124.

Prialnik D. and Bar-Nun A. (1988) *The formation of a permanent dust mantle and its effect on cometary activity*, *Icarus*, *74*, 272–283.

Prialnik D. and Rosenberg E. D. (2009) *Can ice survive in mainbelt comets? Long-term evolution models of comet 133P/Elst-Pizarro*, *Mon. Not. R. Astron. Soc.*, *399*, L79–L83.

Raymond S. N. and Izidoro A. (2017) *The empty primordial asteroid belt*, *Science Advances*, *3*, e1701138.

Rickman H., Fernandez J. A., and Gustafson B. A. S. (1990) *Formation of stable dust mantles on short-period comet nuclei*, *Astron. Astrophys.*, *237*, 524–535.

Rozitis B. and Green S. F. (2013) *The strength and detectability of the YORP effect in near-Earth asteroids: a statistical approach*, *Mon. Not. R. Astron. Soc.*, *430*, 1376–1389.

Rudenko M., Micheli M., Hsieh H. H. et al. (2021) *COMET P/2021 K4 = P/2019 A7 (PANSTARRS)*, *Central Bureau Electronic Telegrams*, *5010*.

Russell C. T., Aroian R., Arghavani M. et al. (1984) *Interplanetary Magnetic Field Enhancements and Their Association with the Asteroid 2201 Oljato*, *Science*, *226*, 43–45.

Ryabova G. O. (2002) *Asteroid 1620 Geographos: II. Associated Meteor Streams*, *Solar System Research*, *36*, 234–247.

Saiki T., Imamura H., Arakawa M. et al. (2017) *The Small Carry-on Impactor (SCI) and the Hayabusa2 Impact Experiment*, *Space Sci. Rev.*, *208*, 165–186.

Sánchez P., Durda D. D., Devaud G. et al. (2021) *Laboratory experiments with self-cohesive powders: Application to the morphology of regolith on small asteroids*, *Planet. Space Sci.*, *207*, 105321.

Sánchez P. and Scheeres D. J. (2014) *The strength of regolith and rubble pile asteroids*, *Meteorit. Planet. Sci.*, *49*, 788–811.

Sarid G., Volk K., Steckloff J. K. et al. (2019) *29P/Schwassmann-Wachmann 1, A Centaur in the Gateway to the Jupiter-family Comets*, *Astrophys. J. Lett.*, *883*, L25.

Scheeres D. J. (2015) *Landslides and Mass shedding on spinning spheroidal asteroids*, *Icarus*, *247*, 1–17.

Scheeres D. J., Hartzell C. M., Sánchez P. et al. (2010) *Scaling forces to asteroid surfaces: The role of cohesion*, *Icarus*, *210*, 968–984.

Schörghofer N. (2008) *The Lifetime of Ice on Main Belt Asteroids*, *Astrophys. J.*, *682*, 697-705.

Schörghofer N. (2016) *Predictions of depth-to-ice on asteroids based on an asynchronous model of temperature, impact stirring, and ice loss*, *Icarus*, *276*, 88–95.

Schörghofer N., Hsieh H. H., Novaković B. et al. (2020) *Preservation of polar ice on near-Earth asteroids originating in the outer main belt: A model study with dynamical trajectories*, *Icarus*, *348*, 113865.

Schultz P. H., Hermalyn B., Colaprete A. et al. (2010) *The LCROSS Cratering Experiment*, *Science*, *330*, 468.

Shannon A., Jackson A. P., Veras D. et al. (2015) *Eight billion asteroids in the Oort cloud*, *Mon. Not. R. Astron. Soc.*, *446*, 2059–2064.

Sheppard S. S. and Trujillo C. (2015) *Discovery and Characteristics of the Rapidly Rotating Active Asteroid (62412) 2000 SY178 in the Main Belt*, *Astron. J.*, *149*, 44.

Simion N. G., Popescu M., Licandro J. et al. (2021) *Spectral properties of near-Earth objects with low-Jovian Tisserand invariant*, *Mon. Not. R. Astron. Soc.*, *508*, 1128–1147.

Smith K. W., Denneau L., Vincent J. B. et al. (2019) *(6478) Gault*, *Central Bureau Electronic Telegrams*, *4594*, 1.

Snodgrass C., Agarwal J., Combi M. et al. (2017) *The Main Belt Comets and ice in the Solar System*, *Astron. Astrophys. Rev.*, *25*, 5.

Snodgrass C., Jones G. H., Boehnhardt H. et al. (2018) *The Castalia mission to Main Belt Comet 133P/Elst-Pizarro*, *Advances in Space Research*, *62*, 1947–1976.

Snodgrass C., Tubiana C., Vincent J.-B. et al. (2010) *A collision in 2009 as the origin of the debris trail of asteroid P/2010A2*, *Nature*, *467*, 814–816.

Sonnett S., Kleyna J., Jedicke R. et al. (2011) *Limits on the size and orbit distribution of main belt comets*, *Icarus*, *215*, 534–546.

Statler T. S. (2009) *Extreme sensitivity of the YORP effect to small-scale topography*, *Icarus*, *202*, 502–513.

Steckloff J. K., Graves K., Hirabayashi M. et al. (2016) *Rotationally induced surface slope-instabilities and the activation of CO_2 activity on comet 103P/Hartley 2*, *Icarus*, *272*, 60–69.

Street R. A., Bowman M., Saunders E. S. et al. (2018) in *Software and Cyberinfrastructure for Astronomy V* (J. C. Guzman and J. Ibsen, eds.), vol. 10707 of *Society of Photo-Optical Instrumentation Engineers (SPIE) Conference Series*, p. 1070711.

Szabó G. M. and Kiss L. L. (2008) *The shape distribution of asteroid families: Evidence for evolution driven by small impacts*, *Icarus*, *196*, 135–143.

Takir D., Kareta T., Emery J. P. et al. (2020) *Near-infrared observations of active asteroid (3200) Phaethon reveal no evidence for hydration*, *Nature Communications*, *11*, 2050.

Tancredi G. (2014) *A criterion to classify asteroids and comets based on the orbital parameters*, *Icarus*, *234*, 66–80.

Taylor P. A., Rivera-Valentín E. G., Benner L. A. M. et al. (2019) *Arecibo radar observations of near-Earth asteroid (3200) Phaethon during the 2017 apparition*, *Planet. Space Sci.*, *167*, 1–8.

Tedesco E. F., Noah P. V., Noah M. et al. (2004) *IRAS Minor Planet Survey V6.0*, *NASA Planetary Data System*, IRAS-A-FPA-3-RDR-IMPS-V6.0.

Tegler S. C., Romanishin W., Consolmagno G. J. et al. (2016) *Two Color Populations of Kuiper Belt and Centaur Objects and the Smaller Orbital Inclinations of Red Centaur Objects*, *Astron. J.*, *152*, 210.

Tholen D., Sheppard S. S., Weryk R. et al. (2021) *Comet P/2021 R8 (Sheppard)*, *Central Bureau Electronic Telegrams*, *5079*.

Tholen D. J., Sheppard S. S., and Trujillo C. A. (2015) in *AAS/Division for Planetary Sciences Meeting Abstracts*, vol. 47, p. 414.03.

Tisserand F. (1896) *Traité de mécanique céleste*, vol. 4, Paris, Gauthier-Villars et fils.

Toth I. (2000) *Impact-generated activity period of the asteroid 7968 Elst-Pizarro in 1996: Identification of the asteroid 427 Galene as the most probable parent body of the impactors*, *Astron. Astrophys.*, *360*, 375–380.

Tsuda Y., Yoshikawa M., Saiki T. et al. (2019) *Hayabusa2-Sample return and kinetic impact mission to near-earth asteroid Ryugu*, *Acta Astronautica*, *156*, 387–393.

Urakawa S., Okumura S.-i., Nishiyama K. et al. (2011) *Photometric observations of 107P/Wilson-Harrington*, *Icarus*, *215*, 17–26.

Vaghi S. (1973) *Orbital Evolution of Comets and Dynamical Characteristics of Jupiter's Family*, *Astron. Astrophys.*, *29*, 85.

Volk K. and Malhotra R. (2008) *The Scattered Disk as the Source*

of the Jupiter Family Comets, Astrophys. J., *687*, 714–725.

Wainscoat R., Weryk R., Cunningham C. et al. (2021) *Comet P/2021 L4 (PANSTARRS)*, Central Bureau Electronic Telegrams, *4986*.

Walsh K. J., Morbidelli A., Raymond S. N. et al. (2011) *A low mass for Mars from Jupiter's early gas-driven migration*, Nature, *475*, 206–209.

Wang J. H. and Brasser R. (2014) *An Oort Cloud origin of the Halley-type comets*, Astron. Astrophys., *563*, A122.

Wang S., Zhao H.-B., Ji J.-H. et al. (2012) *Possible origin of the Damocloids: the scattered disk or a new region?*, Research in Astronomy and Astrophysics, *12*, 1576–1584.

Wang X., Schwan J., Hsu H. W. et al. (2016) *Dust charging and transport on airless planetary bodies*, Geophys. Res. Lett., *43*, 6103–6110.

Warner B., Pravec P., and Harris A. P. (2019) *Asteroid Lightcurve Database (LCDB) V3.0*, NASA Planetary Data System, urn:nasa:pds:ast-lightcurve-database::3.0.

Warren P. H. (2011) *Stable-isotopic anomalies and the accretionary assemblage of the Earth and Mars: A subordinate role for carbonaceous chondrites*, Earth and Planetary Science Letters, *311*, 93–100.

Waszczak A., Ofek E. O., Aharonson O. et al. (2013) *Main-belt comets in the Palomar Transient Factory survey - I. The search for extendedness*, Mon. Not. R. Astron. Soc., *433*, 3115–3132.

Watanabe S., Hirabayashi M., Hirata N. et al. (2019) *Hayabusa2 arrives at the carbonaceous asteroid 162173 Ryugu—A spinning top-shaped rubble pile*, Science, *364*, 268–272.

Weissman P. R. and Levison H. F. (1997) *Origin and Evolution of the Unusual Object 1996 PW: Asteroids from the Oort Cloud?*, Astrophys. J. Lett., *488*, L133–L136.

Weryk R., Wainscoat R., Ramanjooloo Y. et al. (2018) *Comet P/2018 P3 (PANSTARRS)*, Central Bureau Electronic Telegrams, *4548*, 2.

Weryk R., Wainscoat R., Woodworth D. et al. (2019) *Comet P/2019 A3 (Panstarrs)*, Central Bureau Electronic Telegrams, *4598*, 1.

Weryk R., Wainscoat R. J., Wipper C. et al. (2017) *Comet P/2017 S9 (Panstarrs)*, Central Bureau Electronic Telegrams, *4448*, 1.

Weryk R., Wierzchos K. W., Wainscoat R. et al. (2020) *Comet P/2020 O1 (LEMMON-PANSTARRS)*, Central Bureau Electronic Telegrams, *4820*.

Westphal A. J., Fakra S. C., Gainsforth Z. et al. (2009) *Mixing Fraction of Inner Solar System Material in Comet 81P/Wild2*, Astrophys. J., *694*, 18–28.

Whipple F. L. (1950) *A comet model. I. The acceleration of Comet Encke*, Astrophys. J., *111*, 375–394.

Whipple F. L. (1951) *A Comet Model. II. Physical Relations for Comets and Meteors.*, Astrophys. J., *113*, 464.

Wiegert P. A. (2015) *Meteoroid impacts onto asteroids: A competitor for Yarkovsky and YORP*, Icarus, *252*, 22–31.

Wierzchos K. and Womack M. (2020) *CO Gas and Dust Outbursts from Centaur 29P/Schwassmann-Wachmann*, Astron. J., *159*, 136.

Williams I. P. and Wu Z. (1993) *The Geminid meteor stream and asteroid 3200 Phaethon*, Mon. Not. R. Astron. Soc., *262*, 231–248.

Womack M., Sarid G., and Wierzchos K. (2017) *CO in Distantly Active Comets*, PASP, *129*, 031001.

Wong M. H., Meech K. J., Dickinson M. et al. (2020) *Transformative Planetary Science with the US ELT Program*, arXiv e-prints, arXiv:2009.08029.